



19990402 022

ACTIVE MULTISPECTRAL BAND SELECTION
AND REFLECTANCE MEASUREMENT SYSTEM

THESIS

Bradley D. Rennich, Captain, USAF
AFIT/GEO/ENP/99M-01

DEPARTMENT OF THE AIR FORCE
AIR UNIVERSITY
AIR FORCE INSTITUTE OF TECHNOLOGY

Wright-Patterson Air Force Base, Ohio

AFIT/GEO/ENP/99M-01

ACTIVE MULTISPECTRAL BAND SELECTION AND
REFLECTANCE MEASUREMENT SYSTEM

THESIS
Bradley D. Rennich
Captain, USAF

AFIT/GEO/ENP/99M-01

DTIC QUALITY INSPECTED 2

Approved for public release; distribution unlimited

The views expressed in this thesis are those of the author and do not reflect the official policy or position of the Department of Defense or the United States Government.

AFIT/GEO/ENP/99M-01

ACTIVE MULTISPECTRAL BAND SELECTION AND
REFLECTANCE MEASUREMENT SYSTEM

THESIS

Presented to the Faculty of the School of Engineering
of the Air Force Institute of Technology

Air University

In Partial Fulfillment of the
Requirements for the Degree of
Master of Science in Electrical Engineering

Bradley D. Rennich, B.S.E.E.

Captain, USAF

March, 1999

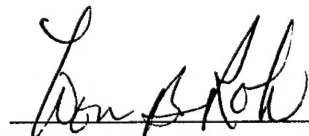
Approved for public release; distribution unlimited

ACTIVE MULTISPECTRAL BAND SELECTION AND
REFLECTANCE MEASUREMENT SYSTEM

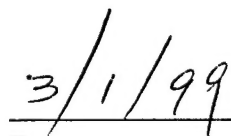
Bradley D. Rennich, B.S.E.E.

Captain, USAF

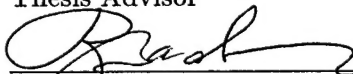
Approved:




Dr. Won B. Roh
Thesis Advisor



Date



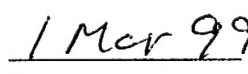
Maj. Patrick J. Gardner
Committee Member



Date



Maj. Michael A. Temple
Committee Member



Date

Acknowledgements

This research could not have been completed without the help of many people. I would like to begin by thanking each of my committee members: my advisor Dr. Roh, Maj Gardner, and Maj Temple. Each one of you provided a great deal of wisdom and support that proved invaluable in the completion of this program. I would also like to thank Eddie, Shaun, and the rest of the guys at the Site C-3, Eglin AFB for the support they gave to me while taking measurements at their facility.

Even more important during this 18 month *vacation* was the love and support my family has given me. I can honestly say that without you, I would not have made it through this rigorous program. A special thanks to my wife, Julie, who continuously put up with late nights and short weekends. And last but certainly not least, I want to thank my two wonderful children: Travis and Bethany. You have provided daddy with many hours of stress relief...many more than you could have possibly caused.

Bradley D. Rennich

Table of Contents

	Page
Acknowledgements	iii
List of Figures	vi
List of Tables	viii
Abstract	ix
I. Introduction	1
1.1 Problem Statement and Scope	2
1.2 Contributions	3
1.3 Thesis Organization	3
II. Multispectral Band Selection	5
2.1 Background	5
2.1.1 NEF Database	5
2.1.2 Band Selection Techniques	6
2.2 Correlation Band Selection Algorithm	7
2.3 Simulations	11
III. BRDF Measurement	16
3.1 Background	16
3.2 Monostatic BRDF Measurement Experiment	19
3.2.1 Experimental Setup	19
3.2.2 Experimental Procedure	21
3.2.3 Data Analysis	22
3.2.4 Error Analysis	24
3.2.5 Results	31

	Page
IV. Optimized Monostatic BRDF Experiment	41
4.1 Overview	41
4.2 Experiment Design	41
V. Conclusions and Recommendations	47
5.1 Conclusions	47
5.2 Recommendations	47
Appendix A. BRDF Data Descriptions	49
A.1 File Names	49
A.2 Data File Format	49
A.2.1 BRDF Data Files	50
A.2.2 Component Calibration and Response Curves	50
Appendix B. BRDF Data	56
B.1 Absolute Method Results	56
B.2 Relative Calibration Method Results	62
Appendix C. Matlab Code for Correlation Band Selection Algorithm	68
C.1 CBand Selection Script	68
C.2 Supporting Functions	72
Bibliography	76
Vita	77

List of Figures

Figure		Page
1.	Material reflectance spectra for four class system	8
2.	Scatterplot of CBand cross-correlation values	10
3.	Two-way atmospheric transmission spectra	12
4.	Selected bands using FSS algorithm	13
5.	Class map after classification using FSS algorithm	13
6.	Selected bands using CBand algorithm	14
7.	Class map after classification using CBand algorithm	15
8.	BRDF geometry	18
9.	Simple BRDF setup	19
10.	Monostatic BRDF measurement setup	20
11.	Layout for BRDF reduction algorithm	24
12.	Absolute Method: SRS-99-010 BRDF data	33
13.	Absolute Method: SRS-99-010 Data (cont.)	34
14.	Absolute Method: B-03 BRDF data	36
15.	Absolute Method: B-03 Data (cont.)	37
16.	Relative Calibration Method: SRS-99-010 BRDF data	39
17.	Relative Calibration Method: B-03 BRDF data	40
18.	Revised monostatic BRDF measurement system	42
19.	Single surface CaF ₂ window reflectance	43
20.	Single surface ZnSe window reflectance	44
21.	Beamsplitter calibration setup	51
22.	Detector calibration setup	52
23.	Pellicle beamsplitter spectral response curves	53
24.	Broadband beamsplitter spectral response curves	54
25.	InGaAs detector spectral response curves	55

Figure		Page
26.	A-Method: SRS-50-010 BRDF data	57
27.	A-Method: Green CARC Paint BRDF data	58
28.	A-Method: B-02 BRDF data	59
29.	A-Method: D-08 BRDF data	60
30.	A-Method: E-38 BRDF data	61
31.	RC Method: SRS-50-010 BRDF data	63
32.	RC Method: Green CARC Paint BRDF data	64
33.	RC Method: B-02 BRDF data	65
34.	RC Method: D-08 BRDF data	66
35.	RC Method: E-38 BRDF data	67

List of Tables

Table		Page
1.	Summary of Correlation Band selection algorithm	11
2.	Sample ID descriptions	50

Abstract

Due to system design requirements, an active multispectral laser radar system may be limited in the number of spectral bands that can be integrated into the system. To aid in the selection of these bands, a novel multispectral band selection technique is presented based on the cross-correlation of the material class reflectance spectra over a wavelength range of $1\mu\text{m} - 5\mu\text{m}$. The algorithm uses directional hemispherical reflectance data from the Nonconventional Exploitation Factors database to select a number of spectral bands for classification purposes.

Because the target material spectral reflectance is so important to the performance of an active multispectral system, an experimental monostatic bidirectional reflectance distribution function (BRDF) measurement system is developed and tested. A $1.06\mu\text{m}$ Nd:YAG diode pumped laser is frequency shifted to $1.58\mu\text{m} - 1.80\mu\text{m}$ using a periodically poled lithium niobate nonlinear crystal. This laser provides the continuously tunable source necessary to measure the material BRDF at closely spaced wavelength intervals. A complete error analysis of the system is presented with measurement results from a number of military vehicle paint samples. An extended design is presented which is capable of operating at any wavelength in the $1\mu\text{m} - 5\mu\text{m}$ micron range. This design also reduces or removes the error sources observed in the initial experiment.

ACTIVE MULTISPECTRAL BAND SELECTION AND REFLECTANCE MEASUREMENT SYSTEM

I. Introduction

Multispectral sensing systems became prominent with the launch of the first Landsat satellite system in 1972. The Multispectral Scanner System (MSS) on-board Landsat 1 provided four spectral bands covering the visible and near-infrared (NIR) regions of the electro-magnetic spectrum(12).

A multispectral sensor system uses the level of radiation sensed in different spectral bands to identify the target. Passive systems rely on radiation that is naturally reflected or emitted by the target. For visible through short wave infrared (SWIR) regions ($0.4\mu\text{m} - 3\mu\text{m}$), the sensed radiation is primarily from reflected solar radiation. Above $5\mu\text{m}$, in the thermal infrared, the collected radiation is generally self-emitted. The mid-wave infrared (MWIR) band from $3\mu\text{m} - 5\mu\text{m}$ is considered a transition region from solar-reflective to thermal emitted.

Materials have surface and atomic properties which cause them to reflect or emit radiation differently making identification possible. Here lies the advantage of using multiple spectral bands; the more spectral features that are known, the better chance of correct identification. The designers of the multispectral systems of today have taken this fact into account and have fielded systems with hundreds of spectral bands.

About the same time that passive multispectral systems were being fielded, researchers were developing a new active system, laser radar. Laser radar, sometimes called LIDAR (light detection and ranging) or LADAR (laser detection and ranging), was originally designed for highly accurate range and direction information. Simply put, a lidar works by actively illuminating a target with laser beam and measuring the round trip time. Because a lidar measures the laser light reflected from a target, its performance is dependent upon the reflectance of the target material.

A merging of these two systems to improve the capabilities of both seemed inevitable. With the merge, a passive multispectral system gains the ability to actively illuminate a target. This frees it for use in low or no light situations. The lidar system adds the ability to use multiple spectral bands to identify targets based on their spectral reflectance properties. Thus the birth of the active multispectral laser radar.

However, design complications arise due to the improvements made to the system. First, passive multispectral systems of today generally contain hundreds of spectral bands. An active multispectral system must be able to produce light in each of the bands sensed. Therefore, an active multispectral laser source must either be tunable across the necessary wavelength range or a separate laser must be incorporated for each wavelength. Even with the recent developments in tunable lasers, a single tunable source is not an option at this time. Nor is it an option to integrate hundreds of discrete wavelength lasers into such a system. This creates a need to find an optimum number and placement of spectral bands in an active multispectral laser radar system to provide confidence in proper target classification.

1.1 Problem Statement and Scope

The Air Force Research Laboratory is currently researching the use of active multispectral laser radar systems for targeting applications. Fielding of such a system requires the tradeoff described above. Ruggedness, size, and cost considerations limit the number of spectral bands available for such a system. This is the basis of the research presented in this document.

This research investigates band selection techniques that choose the best bands to integrate into an active multispectral system given a set of material spectral reflectances. The spectral reflectances are taken from a database of sample material spectra. Once spectral bands are selected, their discrimination ability is tested by building a noisy multiclass, multispectral scene from which each pixel is assigned a class using a Bayes classifier.

Because the spectral reflectance is such an integral part of the active multispectral system (and subsequently the band selection algorithm), a spectral reflectance measure-

ment system is also developed. This system measures the bidirectional reflectance distribution function (BRDF) as a function of wavelength. Such a system is needed to both verify the reflectance of materials already included in the database and also measure the spectral reflectance of materials not currently cataloged.

1.2 Contributions

Key contributions have been made to this field during this research. First, a new multispectral band selection technique based on spectral band correlation was developed. This algorithm, called the correlation band selection algorithm (CBand), uses the cross-correlation of the normalized class reflectances to determine the optimum band pair to select. Once the first band pair is selected, the algorithm uses a newly developed (in this thesis) distance metric to select the remaining number of bands.

Results obtained from this algorithm were compared with another band selection algorithm using a Bayes classifier to assign each pixel of a noisy simulated image to a specific material class. For a four class, three spectral band case, the CBand band selection algorithm provided an overall classification rate which was 10% higher than that of the other band selection algorithm.

Second, specifications for a monostatic bidirectional reflectance distribution function (BRDF) measurement system have been made. These specifications are based on the results observed from testing the initial BRDF measurement system and determining its sources of error. This improved system will provide the user a source for continuously tunable BRDF measurements between $1.5\mu\text{m}$ and $5.0\mu\text{m}$. To the knowledge of this author, this thesis is the first publication that has reported continuously tuned BRDF data. There is, however, at least one system that has used a tunable source to report BRDF data at widely spaced wavelengths(16).

1.3 Thesis Organization

This thesis is organized into five chapters. Chapter II presents current band selection techniques and develops another method based on spectral band correlation techniques.

The outputs of two band selection algorithms are tested using a Bayesian classifier and a comparison of the results is made. Chapter III describes the experimental setup used for the initial monostatic BRDF measurement system, an error analysis, and the results obtained from the system using two different data reduction algorithms. An optimized monostatic BRDF measurement system design is presented in Chapter IV that improves the system performance by removing the sources of error experienced in the initial design. Chapter V summarizes the findings and offers suggestions for further research.

II. Multispectral Band Selection

Multispectral systems can be limited in the number of available or usable spectral bands for a number of different reasons. A passive multispectral system on a satellite, for instance, might be limited by the amount of digital information that can be transmitted to a tracking station. It is also conceivable that a small subset of spectral bands could be chosen from the full set of available bands to reduce the time and cost of the data analysis.

Active multispectral systems, on the other hand, face different restrictions which limit the number of available spectral bands. An active multispectral system may be limited in the number of available laser spectral bands due to system design considerations including ruggedness, size, and cost of the system.

Ideally, correct placement of a few spectral bands in an multispectral system would yield results approximating those found by the use of a full spectral band set. Previous studies(11) have shown that detection performance increases asymptotically with each spectral band added. That is, two bands are better than one, three is better than two, etc. However, each additional band provides a smaller increase in performance and acceptable performance may be obtained with just three or four bands(11).

This chapter begins with a discussion of the Nonconventional Exploitation Factors (NEF) database from which the spectral reflectance values used for the band selection algorithms are taken. It continues with a review of two multispectral band selection techniques reported in literature. Finally, a new band selection technique is described and its results are compared to those obtained from an existing technique by the use of a classification algorithm.

2.1 Background

2.1.1 NEF Database. The NEF Database(9) contains over 600 spectra from many different types of materials including paints, metals, concrete, asphalt, camouflage netting, fabrics and many others. It was developed by the National Imagery and Mapping Agency (NIMA) to provide optical properties for selected materials in support of broadband, multispectral, and hyperspectral sensor systems.

The portion of the NEF database used in this research is the Directional Hemispherical Reflectance (DHR). The DHR is the ratio of the total power reflected by a surface (into the entire hemisphere) to the power incident upon it(9). The DHR contains important spectral information and for this reason it is used in the band selection algorithms. A formal definition of the DHR follows in Section 3.1. The NEF database contains DHR values at $0.02\mu\text{m}$ increments in the spectral range of $1\mu\text{m} - 5\mu\text{m}$ which will be used in the band selection algorithms.

2.1.2 Band Selection Techniques. The goal of band selection algorithms is to choose a specified number of spectral bands that can provide proper material classification in a multispectral imaging system. A number of different techniques to accomplish this task have been reported. Principal component analysis (PCA) is widely used in multispectral and hyperspectral data analysis(2, 10). Maximum likelihood detection using multiband signal to clutter ratio (SCR) has also been reported for passive systems(13). However, two other recently reported techniques will be discussed in this research. The first technique uses a class separability metric based on the within-class and between-class scatter matrices(5). The second method is a correlation based technique used on a single passive multispectral dataset(11). Ideas obtained from the latter technique led to the development of the Correlation Band Selection Algorithm (CBand) introduced in this thesis and described below.

The first technique to be described is a statistical spectral band selection procedure designed for an active multispectral laser radar. As stated above, the algorithm uses a class separability metric based on the within-class and between-class scatter matrices(5). The metric chosen as a measure of this separability is

$$J = \text{tr}(\mathbf{S}_w^{-1} \mathbf{S}_b) \quad (1)$$

where $\text{tr}(\cdot)$ represents the trace operation and \mathbf{S}_w and \mathbf{S}_b represent the within-class and between-class separability matrices. A large J means a large between-class separation relative to the within-class scatter.

The band selection algorithm uses the DHR values from the NEF database for its spectral input. These values can be thought of as mean observation vectors for the classes. In this case, the J metric is essentially the sum of the distance between each class reflectance value and each other class reflectance value for a given spectral band. For instance, consider three material classes in two spectral bands. The classes are denoted as x_i , y_i and z_i where $i = 1, 2$ and denotes the spectral band. The J metric for this case is

$$J = \sqrt{(x_1 - y_1)^2 + (x_2 - y_2)^2} + \sqrt{(x_1 - z_1)^2 + (x_2 - z_2)^2} + \sqrt{(y_1 - z_1)^2 + (y_2 - z_2)^2} \quad (2)$$

A forward sequential feature selection algorithm(4) is used to determine the best bands based on the J metric. The forward sequential search algorithm starts by selecting the band that has the highest individual J value from the full set of candidate bands. Then each remaining band is paired with the first band and the band that produces the greatest J in 2-dimensional space is chosen. Again, each remaining band is paired with the previously chosen bands to choose the band that produces the greatest J value. This step repeats until the required number of bands have been chosen.

The second band selection technique discussed here uses the correlation between spectral bands from multispectral imagery to determine the best bands for material classification(11). The spectral bands are compared by computing the correlation coefficients of the various band combinations. If two bands are perfectly correlated (a correlation coefficient equal to 1) or perfectly uncorrelated (correlation coefficient equal to -1), then there is no real information in them as a pair. However, a correlation coefficient of zero means the bands are randomly correlated and would be good bands to use for classification purposes.

2.2 Correlation Band Selection Algorithm

As an introduction to the correlation band selection algorithm, first consider the four material spectral reflectances shown in Figure 1. What attributes of this data would be helpful in classifying the materials based on a limited number of spectral bands? First, it is desirable that the class reflectances at a selected wavelength be evenly distributed over a

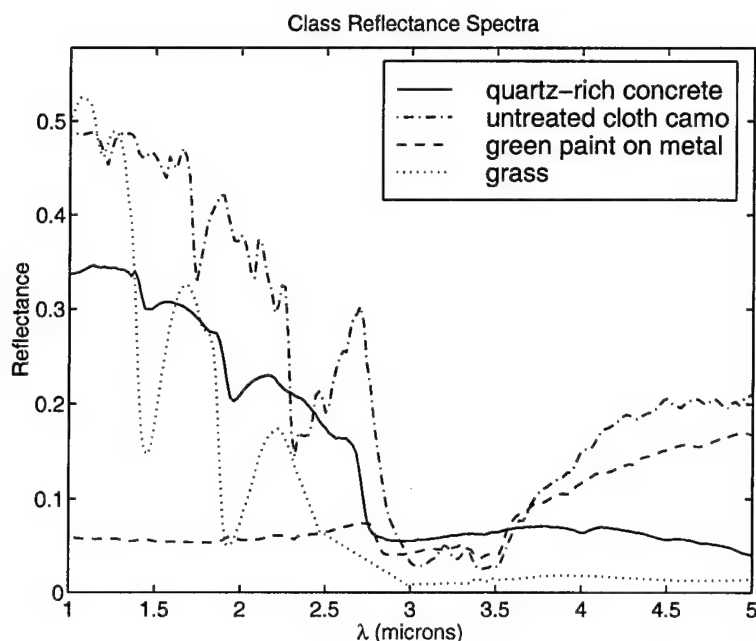


Figure 1 Reflectance spectra for the four material classes used in discussion of Correlation Band selection algorithm. Each material spectrum consists of 201 discrete spectral reflectance values in the interval of $1\mu\text{m} - 5\mu\text{m}$.

wide range of values. The ability of an algorithm to discriminate one class from the others is lost if the reflectances are close to the same value. A second desirable characteristic is that the materials exchange the order of the magnitude of their reflectances. This means that a class that has a low reflectance value at one selected wavelength, has a high reflectance value at another wavelength (compare the reflectance data in the $1.0\mu\text{m} - 1.5\mu\text{m}$ and $4.0\mu\text{m} - 4.5\mu\text{m}$ bands in Figure 1). Having this property in a dataset provides a fingerprint which may help in classification of the materials.

The correlation band selection algorithm (CBand) attempts to identify these properties in a material spectral reflectance dataset. The CBand process starts with the computation of the normalized cross-correlation of each band with every other band. Consider a four material class problem with 200 spectral bands as shown in Figure 1. The normalization step stretches the reflectance values for each band such that the maximum reflectance value for each band is unity. This normalization step is necessary to include spectral bands in which all classes have low reflectance values. Without such normalization, the selected

bands would tend to be the ones with the highest reflectances and not necessarily the ones with the correct properties.

For an L -class case, the normalized cross-correlation can be expressed as

$$C_{i,j} = \frac{1}{L} \sum_{k=1}^L X_{k,i} X_{k,j} \quad (3)$$

where X represents the normalized class reflectance in band i and j for class k , and $0 \leq C_{i,j} \leq 1$.

The lowest $C_{i,j}$ value in the cross-correlation matrix defines the first pair of selected bands. The data in the rows of each of the selected bands can be thought of in 2-dimensions as a scatterplot with the x-axis defined by the cross-correlation with band 1 and the y-axis defined by the cross-correlation with band 2.

It is desirable that the next selected band look as different as possible from the previously selected bands. A graphical representation of this statement is to say that the next selected band should correspond to a point that is as far away as possible from the autocorrelation values of the selected bands. A new distance metric is introduced to accomplish this task. This new selection metric, D , can be expressed mathematically as

$$D_j = \left[\sum_{i=1}^l (C_{b_i,j} - C_{b_i,b_i})^2 \right]^{\frac{1}{2}} \quad (4)$$

where b_i is the i^{th} band of l previously selected bands, and $j = 1, 2, \dots, N$ where N is the total number of spectral bands under consideration.

Figure 2 shows the cross-correlation scatterplot for the 2-dimensional iteration of the CBand algorithm. The point corresponding to the autocorrelation of the first selected pair of bands is plotted as a square in Figure 2. The point on the plot corresponding to the band that provides the maximum metric, D , is shown as a triangle. This is the next (third) spectral band selected by the algorithm.

With three bands selected, the algorithm recomputes the D metric in 3-space to determine the next band to be selected. This process continues with added dimensionality

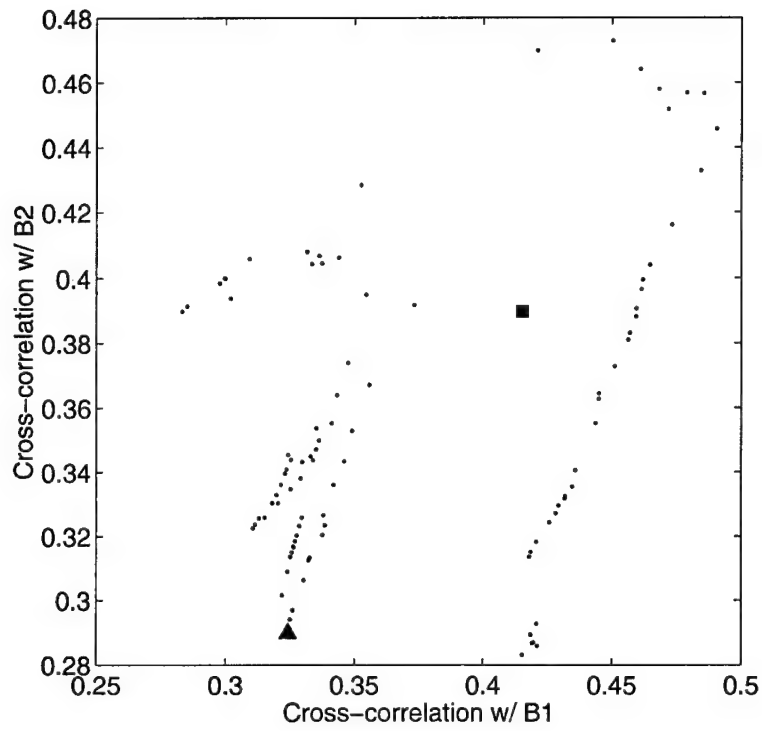


Figure 2 Cross-correlation scatterplot for 2-D iteration of Correlation Band algorithm. The x-axis is defined by the cross-correlation with band 1 and the y-axis is defined by the cross-correlation with band 2. The square represents the auto-correlation of the first pair of bands and the triangle represents the band that provides the largest D metric.

Table 1 Summary of CBand selection algorithm.

Step 1:	Compute the normalized cross-correlation matrix.
Step 2:	Select the band pair with the lowest value in the normalized cross-correlation matrix.
Step 3:	Determine the D metric for the remaining bands and select the band that yields the highest D value.
Step 4:	Repeat Step 3 until the desired number of bands have been selected.

until the specified number of bands have been selected. A summary of the CBand band selection algorithm is presented in Table 1.

With the spectral band selection algorithm in place, one other feature needs to be built into the process to provide more realistic results. Atmospheric attenuation affects the amount of radiation that can be expected from a target. Therefore, it only makes sense for the band selection algorithm to take the atmospheric attenuation into account. The CBand algorithm is designed to only select bands from wavelengths where the transmission through the atmosphere is at least 10%. This prevents the algorithm from selecting spectral bands where there will be no signal due to atmospheric absorption.

Figure 3 shows a typical two-way atmospheric transmission spectra that corresponds to a slant range of 10km and an altitude of 15,000ft under high visibility conditions(5). This data was modeled using moderate resolution atmospheric transmission (MODTRAN).

2.3 Simulations

This section contains a comparison of the band selection algorithm presented by Hardie(5) and the CBand selection algorithm introduced in the present research. The same data will be used in both algorithms and the selected bands will be used to classify a simple noisy scene using a Bayes speckle-Gaussian classifier developed by Hardie(5).

The four material classes shown in Figure 1 are used as the spectral reflectance input and the atmospheric transmission spectra in Figure 3 is used for the atmospheric model. The 5 band set selected using Hardie's forward sequential search method (FSS method) is

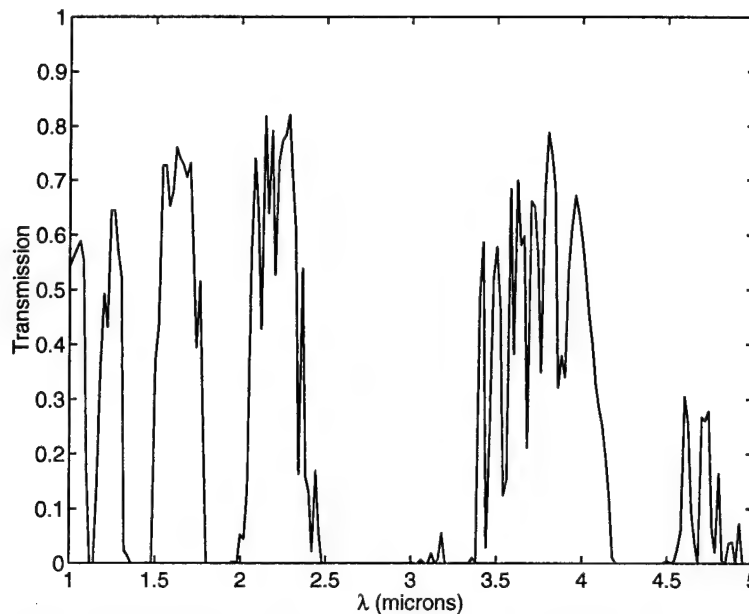


Figure 3 Two way atmospheric transmission spectra for 10km slant range and an altitude of 15,000ft under high visibility conditions(5). Modeled using MODTRAN.

1.26 μ m, 1.54 μ m, 1.24 μ m, 1.66 μ m and 1.06 μ m, given in the order selected. Placement of these bands is shown in Figure 4.

A simulated four class scene was constructed using the first three bands of the five band set of wavelengths. The scene produced was of a simple checker-board pattern with a different class in each quadrant. Speckle noise was then added to each pixel to produce a noisy image to be used for classification. The resulting image was classified, pixel by pixel, using a Bayesian classifier for speckle and Gaussian noise(5). Figure 5 shows the results of the classification process. The overall classification percentage for the four class system was 81%. As can be seen from the class map, the lower left quadrant was classified at 100%. This is important since this quadrant represents the green painted metal which is a valuable material to distinguish from the background clutter.

Examination of Figure 4 explains the perfect classification of the green painted metal class. Note that the reflectance of the green painted metal for each of the first three selected bands (≈ 0.06) is much lower than that of the other three classes (> 0.3). Because speckle noise is multiplicative in nature, the magnitude of the noise added to the image before classification is very low. Subsequently, the large interclass separation of the green painted

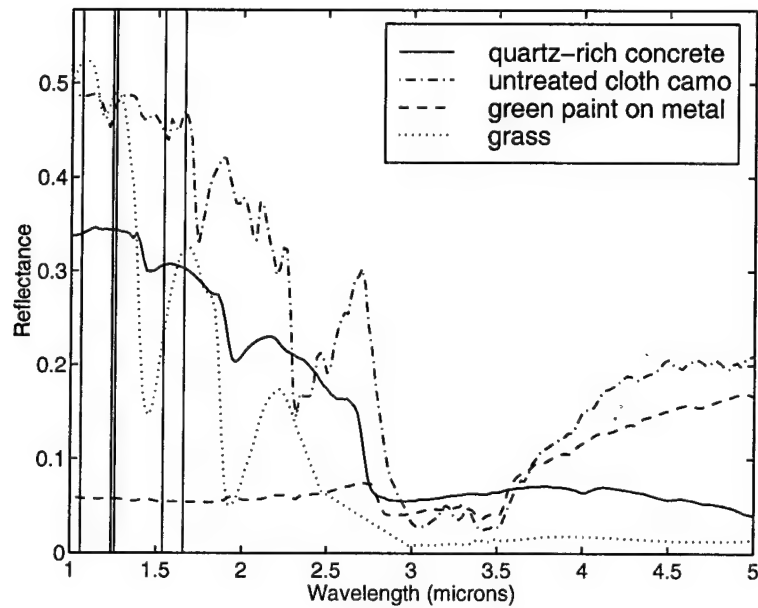


Figure 4 Five band set selected for the four material class problem using the FSS algorithm. Each vertical line corresponds to a selected band.

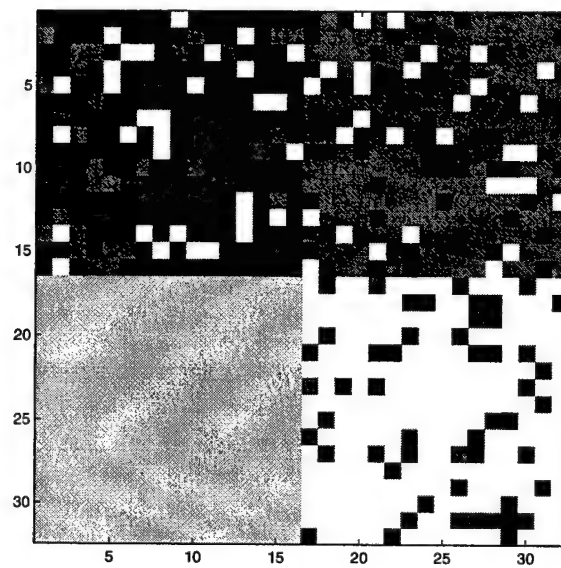


Figure 5 Class map after classification using the first three selected bands from the FSS algorithm. Upper left = asphalt; upper right = camo cloth; lower left = green painted metal; lower right = grass.

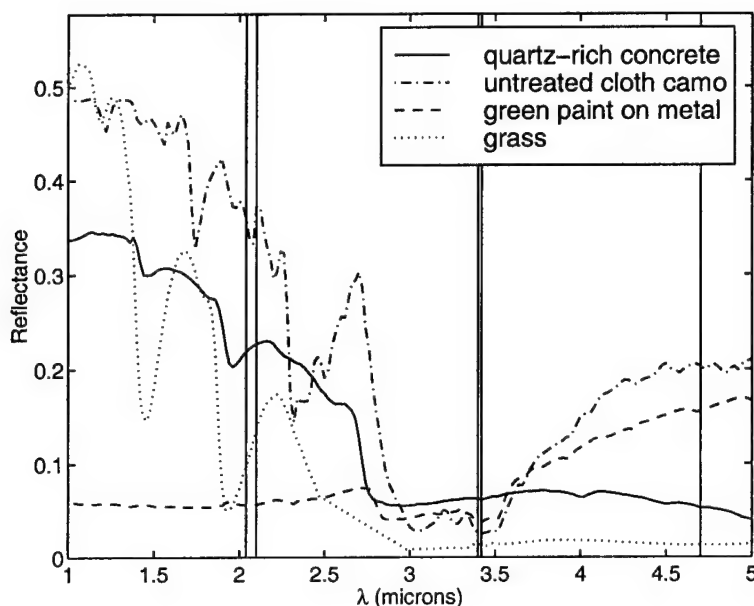


Figure 6 Five band set selected for the four material class problem using the CBand algorithm. Each vertical line corresponds to a selected band.

metal with the other classes and the relatively low green painted metal reflectance combine to produce a high classification rate for the green painted metal.

Using the same input parameters, the CBand selection algorithm selected $4.70\mu\text{m}$, $3.42\mu\text{m}$, $2.04\mu\text{m}$, $3.40\mu\text{m}$ and $2.10\mu\text{m}$ as shown in Figure 6. Notice that these wavelengths are different from those selected by the FSS algorithm. The first three of these are then molded into a scene and speckle noise added to it. Once again, the resulting image is passed to the classifier. Figure 7 shows the result of the classification.

The CBand method showed an overall classification percentage of 90% using three spectral bands. The improvement in classification performance of the CBand algorithm to that of the FSS algorithm for the three band case can be traced to the choice of the third band. The FSS algorithm tends to select a third band which is closely spaced to one of the first pair of bands. Because the third band is so closely spaced to one of the two selected ones, it brings little new information to the classifier and the increase in performance between the two and three band case is small. However, the CBand algorithm is designed to make the third band look spectrally different from the first pair. This was the main

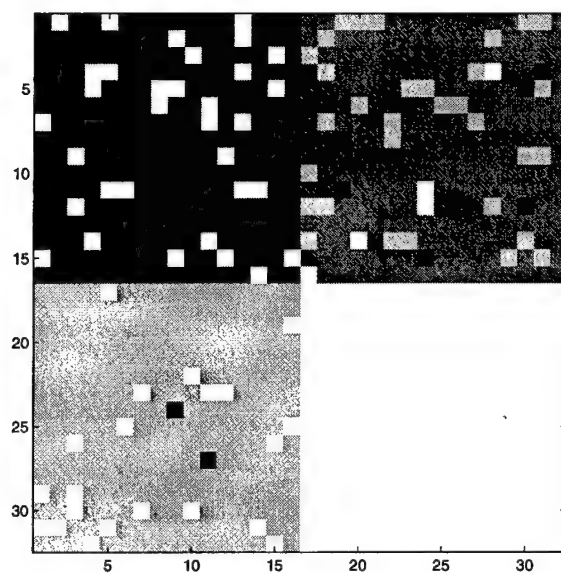


Figure 7 Class map after classification using the first three selected bands from the CBand algorithm. Upper left = asphalt; upper right = camo cloth; lower left = green painted metal; lower right = grass.

design criteria of the D-metric. Therefore the CBand supplies three good spectral bands to the classifier while the FSS algorithm essentially provides only two.

III. BRDF Measurement

There are several types of reflectance measurements that are commonly used for surface reflectance modeling. The bidirectional reflectance distribution function (BRDF) is the most general case from a list which also includes directional hemispherical reflectance and total hemispherical reflectance.

The Air Force Research Laboratory (AFRL) has a requirement for a system that is capable of producing a set of BRDF curves at discrete wavelengths between $1.5\mu\text{m}$ and $5.0\mu\text{m}$. This system would be used to build a database of material BRDF curves that could be used for multispectral system modeling or for band selection codes like those presented in Chapter II. As a proof of concept, the BRDF measurement system described in this chapter is capable of producing BRDF curves at any wavelength in the range $1.58\mu\text{m} - 1.80\mu\text{m}$.

BRDF measurements using this system were performed at the laser radar facility, Site C-3, Eglin AFB, FL. Use of this site was requested by AFRL because of the availability of the tunable laser source described in the experimental section. The choice of some equipment used in the initial setup resulted from the need to use equipment that was in house at the time. This limitation led to problems that are discussed during the error analysis.

This chapter begins with a discussion of the BRDF and how it is related to the directional hemispherical reflectance (DHR). The discussion then turns from the definition of the BRDF to actual BRDF measurement systems. An experimental monostatic BRDF system is presented with an explanation of the measurement procedure and analysis of the data. An error analysis is also presented which details the sources of error in the experimental setup. Finally, BRDF measurement results are given for a number of samples of interest to AFRL using the analysis techniques developed during this research.

3.1 Background

The reflectance of a surface generally depends upon the aspect angle of the source with respect to the aspect angle of the receiver. The BRDF can be thought of as a

specification of this reflectance property. The BRDF, denoted as ρ' , is defined as the ratio of the radiance ($Wm^{-2}sr^{-1}$) reflected into a particular direction to the incident irradiance (Wm^{-2}) per unit area, and has the units of sr^{-1} (15, 9, 14). The BRDF is given by:

$$\rho'(\theta_i, \phi_i, \theta_r, \phi_r; \lambda) = \frac{dL(\theta_r, \phi_r; \lambda)}{dL(\theta_i, \phi_i; \lambda) \cos \theta_i d\omega_i} \quad (5)$$

where θ_i and ϕ_i are the zenith and azimuth angles of the incident radiation and θ_r and ϕ_r are the zenith and azimuth angles of the reflected radiation.¹ This figure is a graphical representation of what happens during the BRDF measurement process. A light source is moved around the hemisphere, as is the detector. For a BRDF to be fully defined for a sample, every possible output angle must be measured for every possible input angle at each wavelength of interest. Then to obtain the spectral characteristics of the material, this process must be repeated for each wavelength of interest. Obviously this would take a great deal of time and effort, so a simplified method will be described in Section 3.2.1. The surface geometry of the BRDF is shown in Figure 8.

The BRDF is the generalized reflectance case from which all other reflectance measurements can be derived(15). It can be used to calculate the DHR by integrating the reflected energy over all angles. The DHR is defined as the ratio of the total power reflected by a surface (into the entire hemisphere) to the power incident upon it(9). The equation for the DHR is given by(15)

$$\rho_d(\theta_i, \phi_i; \lambda) = \int_0^{2\pi} \rho'(\theta_i, \phi_i, \theta_r, \phi_r; \lambda) \cos \theta_r d\omega_r \quad (6)$$

with units of *Watts/Watts* and $0 \leq \rho_d \leq 1$.

Unlike BRDF data, directional reflectance data does not contain any information about the angular distribution of the reflected radiance. DHR data is usually only measured for a single incidence angle and many times the dependence on θ_i and ϕ_i is ignored making

¹Some literature uses s for scatter instead of r for reflection. This difference in notation is meant to be a generalization as scatter can originate from both reflection and transmission. The bidirectional scatter distribution function (BSDF) is defined in this literature in place of the BRDF. For the systems of interest in this research, one is only concerned with the reflected scatter so the BRDF notation will be used throughout.

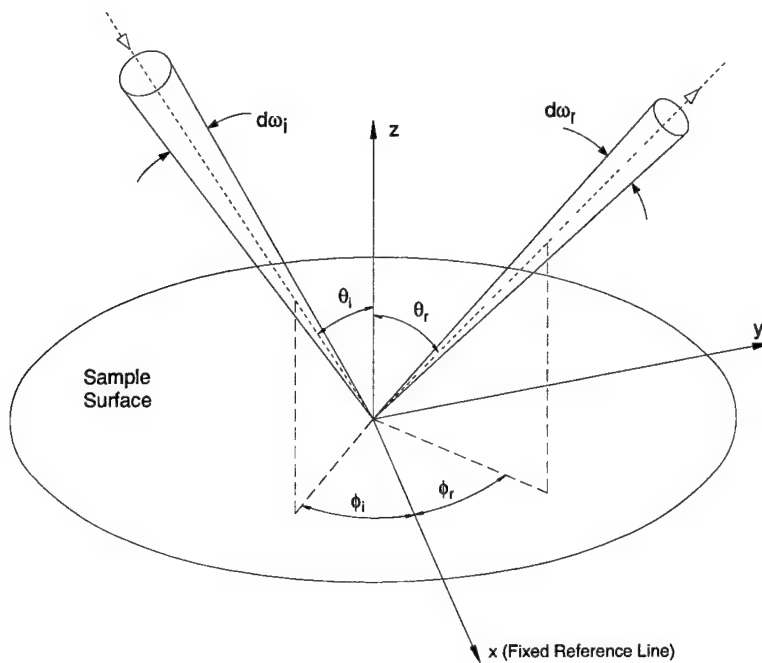


Figure 8 Geometry for the definition of BRDF. (7)

directional reflectance only a function of wavelength. Note that directional reflectance measurements are only truly accurate for surfaces which act as diffuse reflectors.

Now that the quantities of interest are understood, the systems used to measure them can be examined. BRDF measurement systems generally consist of a light source, sample mount, receiver, and electronics(14). One simple system is shown in Figure 9. In this system, a laser beam is used as the light source. It is chopped, spatially filtered, expanded and brought to a focus on the receiver. The scattered light from the sample is collected at the receiver and fed to a lock-in amplifier. The lock-in amplifier uses a reference signal from the chopper to suppress all signals except those at the chopper frequency. Both the optical and the electrical noise are reduced by the use of the lock-in amplifier. The reference detector measures the light scattered off the chopper wheel and is used to correct the scattered signal for fluctuations in laser power.

The sample in this system is placed on a rotation stage which is computer controlled through motion controller electronics. In this way, the computer can coordinate acquisition of data from the reference detector and receiver between sample rotations.

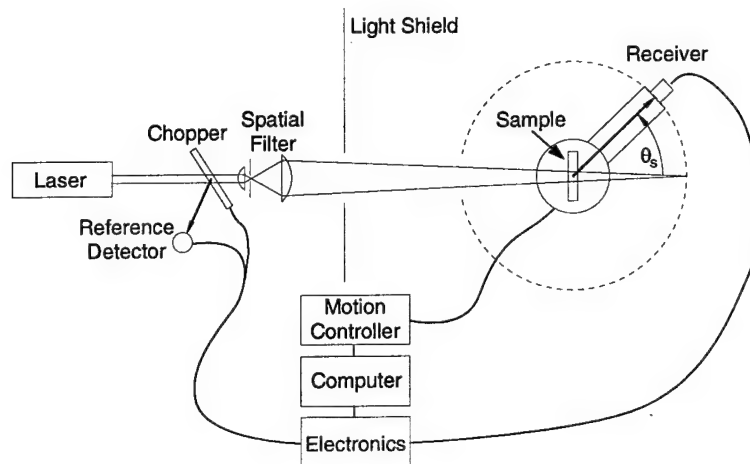


Figure 9 Simple BRDF setup. (14)

The system shown in Figure 9 is an example of a plane-of-incidence scatterometer. It gets its name from the way the receiver moves 360° around the sample. Therefore, for each angle of incidence, the receiver measures the scattered light at each point around the circular path.

This method of BRDF measurement provides more information than is needed for most military applications. Most military systems rely on the power that is reflected directly back at the source. In other words, the light source and receiver are co-located. This leads to the monostatic BRDF measurement system that will be developed now.

3.2 Monostatic BRDF Measurement Experiment

3.2.1 Experimental Setup. A monostatic BRDF measurement system consists of the same basic elements as the scatterometer shown in Figure 9. The main difference is that the transmission aperture and the receiver aperture are co-boresighted. This is accomplished by placing a beamsplitter in the optical path to reflect a portion of the power reflected back from the sample. The experimental configuration used for these measurements is shown in Figure 10.

The source for this experiment is a periodically poled lithium niobate (PPLN) optical parametric oscillator (OPO) pumped by a $1.06\mu\text{m}$, Nd:YAG laser with a 10ns pulse length and 20kHz repetition rate. The laser output consists of three different wavelength regions:

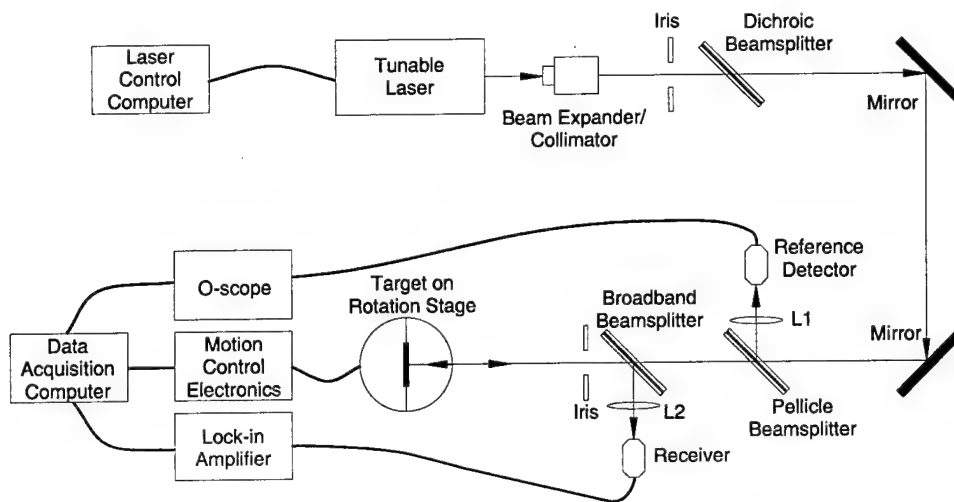


Figure 10 Monostatic BRDF measurement setup.

$1.06\mu\text{m}$ from the pump, the signal beam ($1.58\mu\text{m} - 1.80\mu\text{m}$), and the idler beam ($2.6\mu\text{m} - 3.26\mu\text{m}$). The signal and idler beams are produced when the pump is transformed into two lower energy beams in the PPLN non-linear crystal.² Under this configuration, approximately 40% of the total laser power output is converted to output between $1.58\mu\text{m}$ and $1.80\mu\text{m}$, the range of interest for this experiment.

The output of the tunable laser source is collimated and expanded to produce a 5mm diameter beam. The dichroic beamsplitter removes the $1.06\mu\text{m}$ pump from the beam. The beam is then turned to a pellicle film beamsplitter that reflects approximately 10% of the beam through the lens to be focused on the reference detector as a measure of the incident beam power. The transmitted portion of the beam is incident on a broadband beamsplitter which transmits approximately half of the beam power through the iris and on to the target sample. The sample scatters the beam and returns a portion of it back through the iris aperture and on to the broadband beamsplitter. The light reflected from the broadband beamsplitter is then focused onto the receiver by lens L2.

Indium Gallium Arsenide avalanche photodiodes (InGaAs APDs) were used for both the reference and receiver detectors. The InGaAs detectors have a good response from $0.9\mu\text{m}$ to $1.7\mu\text{m}$ with a responsivity of 9.4A/W at $1.55\mu\text{m}$. The voltage signals from

²A simple explanation of optical parametric oscillation can be found in Hecht(6). A more in-depth coverage of the topic is found in Yariv & Yeh(18).

the reference and receiver detectors are fed into an oscilloscope and a lock-in amplifier, respectively. The data acquisition computer, also doubling as the rotation stage control computer, retrieves the signal values from the oscilloscope and lock-in amplifier and stores them with the input beam angle of incidence.

The target sample is mounted on a tip/tilt stage which in turn is mounted on a computer controlled rotation stage. The tip/tilt control of the sample holder allows fine tuning of the sample alignment once the sample is in place on the rotation stage. The rotation stage is capable of a full 360° of rotation at increments as low as 0.001 degrees per step. The rotation stage control is integrated with the data acquisition computer such that reflectance measurements are taken automatically with each increment in the incidence angle.

3.2.2 Experimental Procedure. This section describes the experimental procedure used for each sample in taking the BRDF measurements. The procedure begins with the mounting of a sample on the sample holder.

The samples studied in this research ranged from 1.5 inch packaged reflectance standards to paint flecks chipped from various military vehicles. Section A.2.1 contains a full description of the samples measured in this research. The reflectance standards were mounted directly to the sample holder while the paint flecks were mounted to a glass slide prior to attaching to the sample holder. The glass slide provides both a stable platform for measurement and also protects the paint flecks during handling and storage.

Once the slide is attached to the sample holder, the tunable source is set to $1.58\mu\text{m}$ and turned on. The sample alignment is then fine tuned to ensure that the beam is incident on the middle of the sample and that the beam stays on the sample through the entire rotation range. Care is also taken to ensure the sample is situated perpendicular to the incident beam both horizontally and vertically at 0° incidence.

After sample alignment is complete, the acquisition/rotation control computer is set to measure the reflected signal -45° to 45° from normal incidence in 1° increments at the current wavelength. Once the acquisition process starts, the acquisition computer moves the rotation stage to 45° and records the measured reference and receiver signal at each

angle of incidence. The measured signals are stored to disk after the rotation sequence is complete.

The laser control computer is set to increment the wavelength by $0.02\mu\text{m}$ and data is again acquired at each angle of incidence. This repeats until a full sequence of reference and receiver signals are recorded at each angle and wavelength. For this research, data was collected from $1.58\mu\text{m}$ to $1.80\mu\text{m}$ at $0.02\mu\text{m}$ increments.

3.2.3 Data Analysis. In this section, two BRDF data analysis techniques will be described for the data produced in the monostatic BRDF experimental measurement system. The first will be an absolute measurement method (A-method) in which a full spectral calibration of the optics is used to radiometrically characterize the system and back out all the parameters needed for the calculation of the BRDF. The second method uses a known, calibrated reflectance standard to produce a spectral correction factor to apply to the data. This method will be called the relative calibration method (RC method). The results obtained from both methods of analysis are shown in Section 3.2.5.

For both methods, the following assumptions are needed to simplify the analysis:

- The incident beam is nearly collimated.
- The incident beam has a uniform cross section.
- The sample surface is isotropic.
- All reflection comes from the sample surface and none from the bulk of the material.

BRDF Measurement System Data Analysis. The A-method begins with the definition of the BRDF as given in Eq. 5. With the assumptions listed above, the BRDF expression becomes(14)

$$\rho' \equiv \frac{\text{differential radiance}}{\text{differential irradiance}} \simeq \frac{dP_r/d\Omega_r}{P_i \cos \theta_r} \simeq \frac{P_r/\Omega_r}{P_i \cos \theta_r} \quad (7)$$

where P_r is the power reflected from the sample through the solid angle subtended by the receiver aperture, Ω_r . P_i is the incident beam power and θ_r is the angle between the sample surface normal and the receiver aperture. P_r , Ω_r and θ_r are all measured quantities

in this experiment. Only P_i is not known directly (and cannot be measured directly in a continuous fashion). It can, however, be determined from the spectral response curves of both the pellicle and broadband beamsplitters and the reference detector output.

Figure 11 contains the critical parts of the system in terms of data analysis and is used to step through the data analysis process. A starting laser beam power of P_1 is assumed. The portion of the initial beam power which is incident on the sample is determined by the spectral response curves of both the pellicle beamsplitter and the broadband beamsplitter as given by

$$\begin{aligned} P_i &= P_1 T_{pell} T_{bbs} \\ &= P_1 (1 - R_{pell}) T_{bbs} \end{aligned}$$

where P_i is the beam power incident on the sample, P_1 is the beam power just before the pellicle beamsplitter, T_{pell} is the transmission of the pellicle beamsplitter and T_{bbs} is the transmission of the broadband beamsplitter. The spectral response curves for each of the beamsplitters is shown in Figure 23 and Figure 24 in Appendix A.2.2.

However, P_1 is known in terms of the power measured by the reference detector, P_{ref} , and the reflectance of the pellicle beamsplitter, R_{pell} (i.e. $P_1 = \frac{P_{ref}}{R_{pell}}$). Making this substitution and simplifying leads to the following expression for P_i .

$$P_i = \left(\frac{1}{R_{pell}} - 1 \right) P_{ref} T_{bbs} \quad (8)$$

Now, Eq. 7 can be expressed totally in terms of known or measured values. Combining Eq. 7 and Eq. 8 leads to the BRDF expression used for the first method of data reduction.

$$\rho' = \frac{P_r}{\left(\frac{1}{R_{pell}} - 1 \right) P_{ref} T_{bbs} \Omega_r \cos \theta_r} \quad (9)$$

Relative Calibration Data Analysis Method. The second method of data reduction is a simple relative method which uses a calibrated reflectance standard to calibrate the system. This method was developed to remove the reliance of the data reduction al-

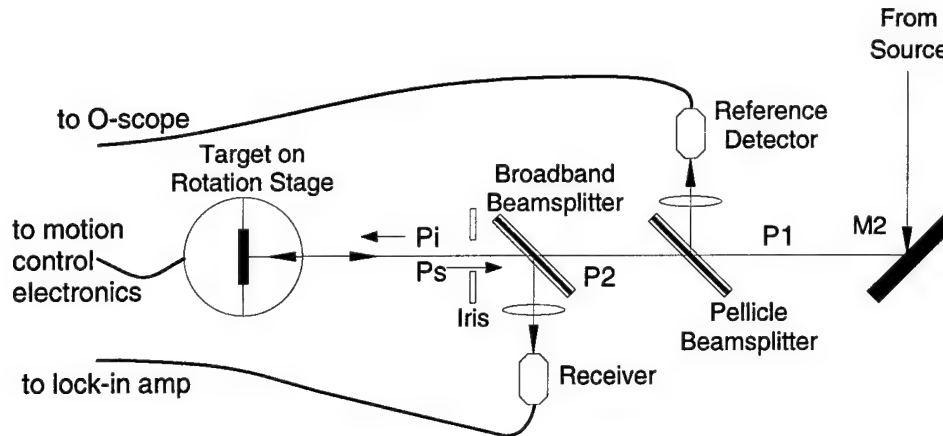


Figure 11 Layout for BRDF reduction algorithm.

gorithm on the pellicle beamsplitter response curves and the reference detector signal. In this case, a calibrated Labsphere SRS-99-010 reflectance standard was used as the calibration source. This standard is specified to be a diffuse reflector and spectrally flat to $\pm 4\%$ between $0.2\mu\text{m}$ and $2.5\mu\text{m}$.

The raw receiver signal from the SRS-99-010 data set was taken, cosine corrected for the incident beam angle, and averaged to produce a single correction value at each wavelength. This value was again corrected such that when applied to the raw receiver signal, would produce a BRDF value at $0.99/\pi$. This correction factor was then applied directly to the other sample data sets to provide the same correction.

Two forms of data analysis have now been described, one complex and one relatively simple. With the description of these now complete, a discussion of the errors involved with each method now follows.

3.2.4 Error Analysis. This section contains an error analysis of the BRDF measurement system. Generally, error analysis is performed to improve the confidence in the results of an experiment or in the case of a failed experiment, to explain the sources of error encountered and suggest methods to overcome them in future experiments. The error analysis presented here first discusses the error sources for this experiment. Then a conventional error analysis is completed in the second part of this chapter to present the error propagation equation for the BRDF measurement system. Finally, error sources for the

second method of data analysis, relative calibration method, will be discussed. Solutions to the problems discussed below will be deferred to Chapter IV for the presentation of the redesigned BRDF measurement system.

Error Sources of BRDF Measurement System. The following is a list of error sources in order of severity that have been discovered for the BRDF measurement system. Each item in the list will be explained for its prevention in future measurements of this kind. This list will also help in interpreting the BRDF measurement results presented in Section 3.2.5. The error sources discovered for this BRDF measurement system are:

- Pellicle beamsplitter
- Detector saturation and non-linearity
- Detector wavelength cutoff
- Pellicle and broadband beamsplitter transmission curves
- Reflected signal errors due to polarization
- Differences in lock-in amplifier and oscilloscope measurements
- Uncertainty in detector overfill
- Non-uniformity of beam
- Laser wavelength variations
- System misalignment
- Measurement error in aperture size and distances

While the pellicle beamsplitter has some attractive properties, is not a good choice for this kind of measurement. It is constructed by stretching a $5\mu\text{m}$ thick membrane over a flat metal frame. The pellicle beamsplitter has a very favorable 8% average reflectivity over a wide wavelength range and virtually no secondary reflections because of its extreme thinness. The problem with the pellicle beamsplitter is that its spectral response curve contains a $\pm 5\%$ sinusoidal oscillation in the transmitted beam due to interference effects between reflections from the front and back surfaces. This results in the ripple in the response curves in Figure 23 in Appendix A.2.2. The problem with the ripple comes about

because the data reduction equation, Eq. 9, has the spectral reflectance of the pellicle beamsplitter in the denominator. This causes a multiplication factor of about 70 at $1.64\mu\text{m}$ while only 8 at $1.76\mu\text{m}$.

The second major source of error in the system was due to reference detector saturation. Recall that the pellicle beamsplitter reflects 8% of the beam into the reference detector. The beam power incident on the pellicle beamsplitter was measured at 75mW. This would mean about 6mW of power is incident on the reference detector, well within its linear range of operation. However, the 75mW is average power from a laser which is producing 20ns pulses at 20kHz. This means that the peak power is approximately 15W which is well out of the linear range of the detector.

The InGaAs detectors used were not the best detectors for the experiment. Although they had the required bandwidth and excellent responsivity, they had a cutoff wavelength of $1.7\mu\text{m}$ while the rest of the experiment was designed to work to $1.8\mu\text{m}$. The cutoff wavelength can easily be observed in the measured detector response shown in Figure 25 in Appendix A.2.2.

Another issue with the detectors was the active sensor area. Each detector had an active diameter of $80\mu\text{m}$. However, the spot size on the receiver was $260\mu\text{m}$ in diameter so the detector was overfilled. Ideally, this does not pose a problem if the incident beam has a uniform cross-section and the sample is isotropic. However, the incident beam is not perfectly uniform and the samples are not perfectly isotropic. The incident beam was made as uniform as possible by over-expanding the collimated beam and stopping it down to the desired diameter. An attempt was made to spatially filter the beam to clean it up even more, however, the beam contained too much power and burned holes through the spatial filter.

The beamsplitter spectral response curves were measured according to the procedure outlined in Appendix A.2.2. Unfortunately, this calibration measurement was made with an unpolarized source while in the the BRDF measurement system, the incident beam was *s*-polarized. Because the calibration was made with unpolarized source, the curves shown are actually an average of the *p*-polarized light and the *s*-polarized light. This introduces

error into both the power incident on the sample and also the power reflected off the sample and then reflected off the broadband beamsplitter into the receiver.

The next source of error is related to the previous discussion. With proper measurement of both the s and p polarization components of the beamsplitter transmission, the proper incident beam power can be determined. However, the power reflected from the sample may have any polarization. This poses a problem in determining the proportion of the reflected sample power that is reflected to the receiver by the broadband beamsplitter. Under the configuration presented in Figure 10, there is no way of determining what beamsplitter reflectance to use. This problem is addressed in the improved design presented in Chapter 4.

The use of a lock-in amplifier for measurement of the receiver channel signal while using an oscilloscope for the measurement of the reference channel signal proved to be another problem. Differences in the measurement technique between the two devices led to a different measured signal value for the same signal. This is easily corrected by having identical electronics in both the receiver and reference channels.

Although the laser source wavelength is computer controlled, there is no active feedback to verify the laser output is at the wavelength stated on the computer screen. Any shift in the laser wavelength from that entered into the laser control computer produces a corresponding shift on the spectral response curves of the beamsplitters. If it were not for the ripple in the pellicle response, this shift would produce a negligible amount of error. However, this error could become noticeable with the rapidly changing beamsplitter response due to the interference caused by the pellicle beamsplitter. Placement of a monochromator in the BRDF measurement system would verify the wavelength and also provide a measurement of the linewidth to the results.

The last two error sources are ones that cannot be totally eliminated, but can be minimized by careful setup and measurement. Errors due to system misalignment, includes things like samples not being mounted perpendicular in both the horizontal and vertical directions, beamsplitters not at exactly 45° in either the BRDF measurement system or during calibration, or even the receiver not being exactly centered on the oversized reflected

signal spot. All these little misalignments cause errors that add to the total error of a measurement. The best that can be done is to identify the places where these types of errors can occur and minimize them.

Errors in measurements of the solid angle can make for extremely large errors in the BRDF measurement, especially for surfaces that have highly specular reflectances. This is because the maximum possible BRDF reflectance is equal to $1/\Omega_r$, the inverse of the solid angle subtended by the receiver. This can be observed in Eq 9. Consider a purely specular sample at normal incidence ($\theta_i = 0$) such that $P_r = P_i$. The measured BRDF for that point is $\rho' = 1/\Omega_r = 1775\text{sr}^{-1}$ for the aperture used in the BRDF measurement system. A 1% reduction in the diameter of the aperture (about .38 mm) changes the measured BRDF to 1810sr^{-1} . Obviously, the smaller the solid angle gets, the more important it is to accurately measure it. However, errors in measurement of the solid angle equally affect all data taken with this system so if relative changes in BRDF are all that is important, this error is irrelevant. However, this error does become a problem when comparing results with another system or when the absolute magnitude of the BRDF is important.

Conventional Error Analysis of BRDF Measurement System. Now that the error sources of the experiment have been presented, a short discussion of the error propagation is presented. The conventional error analysis begins with the BRDF data reduction equation given in Eq 9.

$$\rho' = \frac{P_r}{\left(\frac{1}{R_{pell}} - 1\right) P_{ref} T_{bbs} \Omega_r \cos \theta_r} \quad (9)$$

The error propagation equation for a function, $x = f(u, v)$, is given by(1)

$$\sigma_x^2 \simeq \sigma_u^2 \left(\frac{\partial x}{\partial u}\right)^2 + \sigma_v^2 \left(\frac{\partial x}{\partial v}\right)^2 + 2\sigma_{uv} \left(\frac{\partial x}{\partial u}\right) \left(\frac{\partial x}{\partial v}\right) \quad (10)$$

where σ_x^2 , σ_u^2 and σ_v^2 are the variances for the function x and variables u and v , respectively and σ_{uv} is the covariance between the variables u and v . If the fluctuations in the measured quantities u and v are uncorrelated, σ_{uv} goes to zero and the third term in Eq. 10 falls out

of the expression leaving

$$\sigma_x^2 \simeq \sigma_u^2 \left(\frac{\partial x}{\partial u} \right)^2 + \sigma_v^2 \left(\frac{\partial x}{\partial v} \right)^2 \quad (11)$$

The measured quantities in Eq. 9 are independent random variables for this experiment. Because being independent implies being uncorrelated(17), the covariance terms go to zero and the result is in the form of Eq. 11. Adapting this expression for Eq. 9 yields the following:

$$\begin{aligned} \sigma_{\rho'}^2 \simeq & \sigma_{P_r}^2 \left(\frac{\partial \rho'}{\partial P_r} \right)^2 + \sigma_{P_{ref}}^2 \left(\frac{\partial \rho'}{\partial P_{ref}} \right)^2 + \sigma_{T_{bbs}}^2 \left(\frac{\partial \rho'}{\partial T_{bbs}} \right)^2 \\ & + \sigma_{R_{pell}}^2 \left(\frac{\partial \rho'}{\partial R_{pell}} \right)^2 + \sigma_{\Omega_r}^2 \left(\frac{\partial \rho'}{\partial \Omega_r} \right)^2 + \sigma_{\theta_r}^2 \left(\frac{\partial \rho'}{\partial \theta_r} \right)^2 \end{aligned} \quad (12)$$

Evaluating the partials and simplifying this expression yields the expression for the relative error

$$\frac{\sigma_{\rho'}}{\rho'} \simeq \left[\frac{\sigma_{P_r}^2}{P_r^2} + \frac{\sigma_{P_{ref}}^2}{P_{ref}^2} + \frac{\sigma_{T_{bbs}}^2}{T_{bbs}^2} + \frac{\sigma_{R_{pell}}^2}{R_{pell}^2 (1 - R_{pell})} + \frac{\sigma_{\Omega_r}^2}{\Omega_r^2} + \sigma_{\theta_r}^2 \tan^2 \theta_r \right]^{\frac{1}{2}} \quad (13)$$

Term by term examination of Eq. 13 highlights the measured quantities that contribute the most to the relative error in the BRDF measurement experiment. For easier understanding and explanation, the square of Eq. 13, $\left(\frac{\sigma_{\rho'}}{\rho'} \right)^2$, will be used.

First the measured reflected power term, P_r . This term could contribute significantly to the relative error of the experiment, especially for diffuse surfaces where the power is evenly scattered in all directions. Under this condition, the reflected power collected by the receiver could be on the order of microwatts making noise reduction in this channel very important. This is contrasted with the second term, P_{ref} which is a relatively high power part of the beam path. On average, P_{ref} contains about 5% of the original beam power making it's component a low contributor to the overall relative error.

The effects of the beamsplitter responses show the same contrast. The broadband beamsplitter transmission is close to 50% which when calculated contributes only about four times the variance in T_{bbs} to the expression. The pellicle reflectance, on the other

hand, gets as low as 2%. At this level, it can contribute 2550 times the variance in its measurement to the expression, 600 times that of the broadband beamsplitter for the same variance. For this reason, it is important to know the pellicle beamsplitter reflectance to a very high accuracy.

It is also important to measure the solid angle subtended by the receiver with high precision. Because the solid angle tends to be a very small quantity, any errors in its measurement can contribute greatly to the relative error in the system. This error can be kept small by careful measurement of the both receiver aperture and the distance from it to the sample.

The last term, θ_r , is another term that contributes very little to the total relative error in the measurement. This especially holds true for the angles of interest in this research. At 45° , the largest angle of interest, $\tan^2 \theta_r = 1$ leaving only the variance in the measurement of the angle as the contribution to the expression. It should be noted that this term does become important as the sample angle approaches 90° .

This analysis has provided the areas of the experiment that need to be monitored to keep the experimental error to a minimum. The important measurements are the power reflected into the receiver, the reflectance of the pellicle beamsplitter, and the solid angle subtended by the receiver. Proper measurement of all the quantities with special attention paid to these will ensure good measurement results.

Error Analysis of Relative Calibration Method. The error analysis for the relative calibration method includes many of the same error sources as discussed above. However, some sources of error are removed or reduced because they have been divided out in the correction process. A brief overview of the error sources that may affect the results for this analysis method will now be discussed.

The largest problem with the relative calibration method is that laser power variations are not accounted for. If the power output of the laser changes at all from the calibrated sample data run to the sample data run, error is introduced. One must remember the reason this method was developed was to remove the reliance on the reference

signal due to saturation of the reference detector and the sinusoidal response curve of the pellicle beamsplitter.

The other major problem with this method is that the calibration is made to a diffuse reflector. This calibration does a good job for samples that are somewhat diffuse but is expected to be less accurate for samples that have a more specular reflectance. There are a couple of reasons to expect reduced performance for specular reflectors. First, specular components tend to have higher signal levels. For strongly specular surfaces, there may be many orders of magnitude difference in their signal levels compared to that of a diffuse reflecting surface. Secondly, diffuse reflectors tend to produce unpolarized reflected radiation unlike a specular reflector which tends to keep the same polarization. Any change in the polarization from the diffusely reflected case will cause some error due to the polarization properties of the broadband beamsplitter.

The uncertainty in the amount of detector overfill is removed since the system alignment does not change. Non-uniformity of the beam and any laser wavelength variations produce the same result as described above. Collectively, the number and severity of the error sources observed with the relative method of data analysis is less than that of the absolute method. This is mainly due to the removal of the pellicle beamsplitter and the reference signal from the reduction method.

3.2.5 Results. This section contains a sample of the results obtained from the monostatic BRDF measurement system. A full set of results can be found in Appendix B. Sample results for both analysis methods are presented and the strengths and weaknesses of each method are discussed. The first of the two samples chosen for this section is a Labsphere SRS-99-010 reflectance standard. This is a 1.25 inch diameter diffuse reflectance standard with a 99% reflectance factor. The reflector is specified to be spectrally flat to $\pm 4\%$ over the range of 0.2 to $2.5\mu\text{m}$.

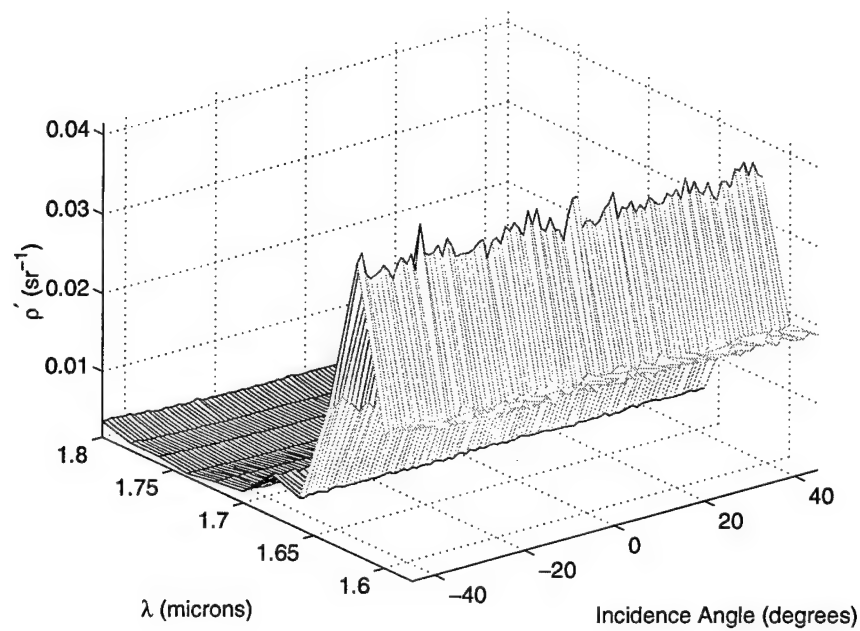
Results from Absolute Method. Figure 12(a) shows the BRDF of sample SRS-99-010 using the absolute method of data analysis. Figure 12(b) is a semilog plot of the same BRDF data to emphasize the magnitude of the BRDF as a function of wavelength.

Figure 13(a) and (b) show the raw measured signal voltages from the receiver and reference detectors, respectively. There are many things to take note of in these plots. First, note the detector falloff, especially in the receiver channel of Figure 13(a). Past $1.74\mu\text{m}$, there is very little signal; not enough to place any confidence in a measurement. The reference channel however (see Figure 13(b)), has an abundance of signal, even at $1.8\mu\text{m}$ where the responsivity of the InGaAs detectors is very low. The sinusoidal response of the pellicle beamsplitter is also apparent in the reference detector output voltage.

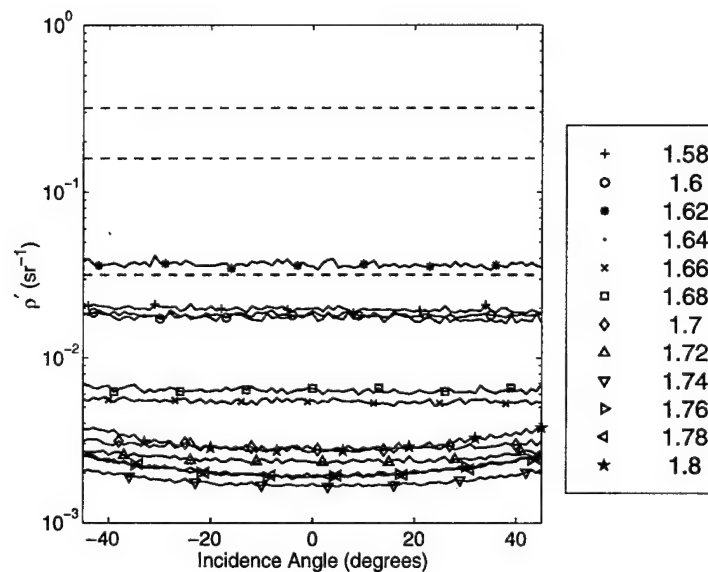
One can also see the effects of the pellicle beamsplitter response in the receiver and reference detector signal voltage plots. The peak of the receiver curve corresponds exactly to the valley of the reference curve, and they both match, with a slight shift, the pellicle beamsplitter spectral response. Experimentally, the minimum pellicle beamsplitter reflectance is observed at $1.62\mu\text{m}$ while during calibration, the minimum reflectance is at $1.64\mu\text{m}$ as seen in Figure 23. It is theorized that this is due to a slight difference in rotation of the beamsplitter from the calibration phase to the experimental phase.

Because the surface acts as a diffuse reflector, the measured BRDF for this sample should be $1/\pi$. Figure 12(a) shows that this is not the case. This fact is not surprising because of the problems experienced in the experiment as discussed in the error analysis. So what can be said about the data? The reduced ρ' data is definitely flat across all sample angles (Figure 12(b)). This means that the sample is a highly diffuse reflector. Obviously, one problem with the data is that the values at each wavelength are not what they should be. This is a manifestation of the errors discussed in the error analysis.

Another problem with the data is noise. Notice the roughness of the BRDF plots in Figure 12(a), especially at $1.62\mu\text{m}$. This is due to the way data was collected in the reference channel. A single instantaneous measurement point was taken from the oscilloscope for each sample angle. Each of these points is used in the data reduction algorithm and ultimately cause the noise observed in the results. The same noise is observed in the reference detector signal of Figure 13(b). Better results from this method of analysis would have led to a method of applying a sliding window average to the reference signal to lessen this effect.

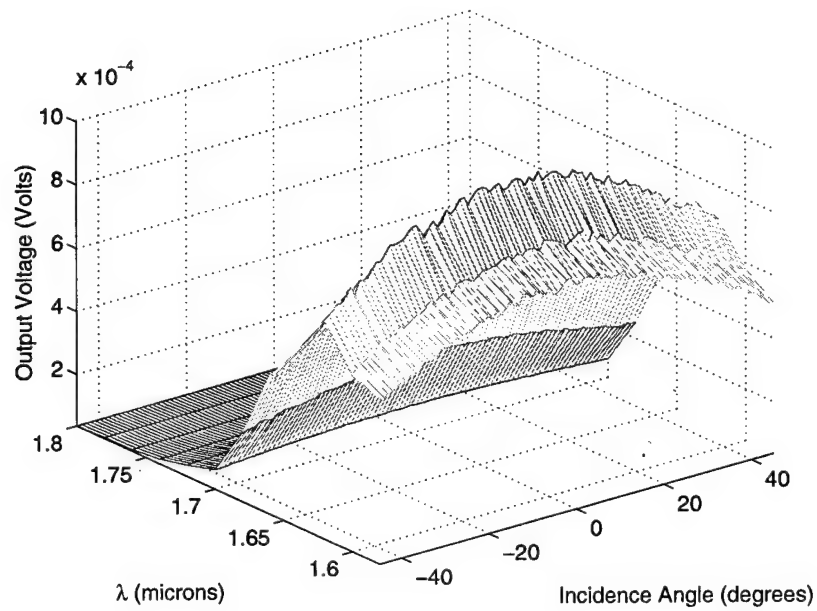


(a)

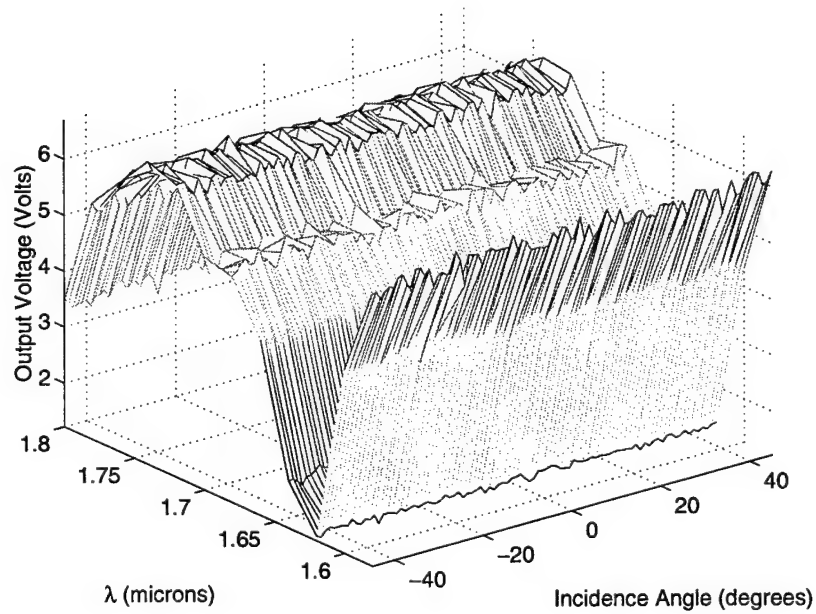


(b)

Figure 12 SRS-99-010 BRDF data using the absolute method of data analysis. (a) Mesh plot of BRDF data. Data points at one degree increments between -45 degrees and 45 degrees along the incidence angle axis. Data points at $0.02\mu\text{m}$ intervals between $1.58\mu\text{m}$ and $1.8\mu\text{m}$ along the λ axis. (b) same BRDF data in semilog format to emphasize spacing of ρ' as a function of wavelength. The dashed lines represent the BRDF for a diffuse surface with 100%, 50% and 10% reflectance factor.



(a)



(b)

Figure 13 SRS-99-010 raw BRDF data. (a) Raw receiver signal voltage measured at one degree increments between -45 degrees and 45 degrees along the incidence angle axis and at $0.02\mu\text{m}$ intervals between $1.58\mu\text{m}$ and $1.8\mu\text{m}$ along λ axis. (b) Raw reference detector voltage measured concurrently with the signal voltage in (a).

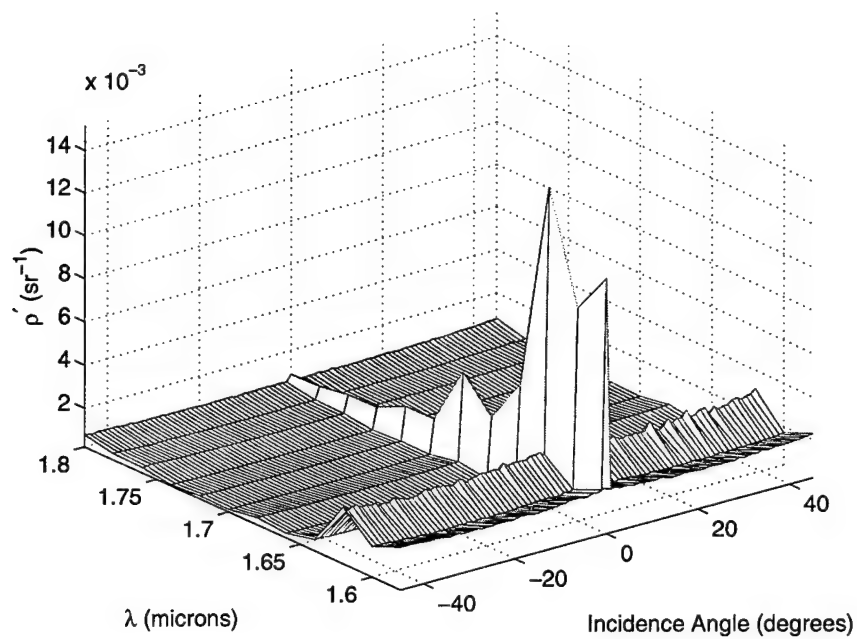
The second sample presented in this section is of Sample ID: B-03. Appendix A.2.1 contains a table matching the paint sample identifications to the vehicles from which they were taken from. B-03 is a large single green paint chip with a dull, rough texture.

Figure 14 shows the measured BRDF for this sample, again using the absolute method of data analysis. These plots show that this sample has a sharp specular reflection component at normal incidence. This specular component is strong enough to show itself at $1.8\mu\text{m}$. Away from normal incidence, the surface has properties that are distinctly diffuse. The unique properties of this sample provide a definite contrast to those observed in the SRS-99-010 data.

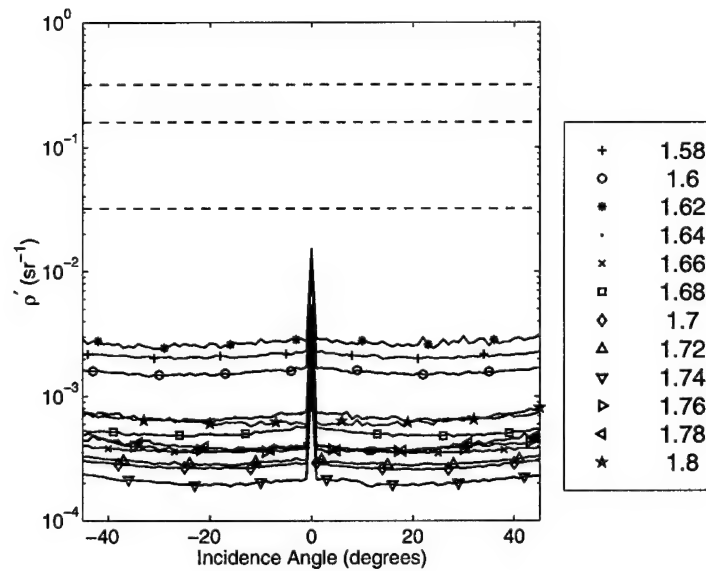
The raw receiver and reference voltage plots in Figure 15 are included for comparison with those from SRS-99-010 in Figure 13. The B-03 reference voltage (Figure 15(b)) shows a slightly different voltage response from that of the SRS-99-010. This difference is probably caused by either a slight shift in the laser wavelengths between the two runs or a slight rotation of the pellicle beamsplitter.

Overall, the A-method of data analysis provides little information about the reflectance properties of a sample. The one thing that can be determined is whether the sample is a diffuse or specular reflector and to what degree. An example of each type was shown in the samples presented here. Differing degrees of these extremes can be found in the full data set in Appendix B. The A-method does not provide any information about how the reflectance properties of the sample change with wavelength or the percent reflectance of the sample surface. This is a result of the reference detector saturation and the ripple in the pellicle beamsplitter spectral response. This is unfortunate because of the purity of the theory that resulted in the formulation of this analysis method.

Results from Relative Calibration Method. Now the same two samples will be re-analyzed using the relative calibration (RC) method of data analysis. First, the SRS-99-010 sample is examined. The data collected from the SRS-99-010 reflectance standard is used to determine the correction factor to apply to the data. Due to a low signal to noise ratio above $1.68\mu\text{m}$, the RC-method is only used to evaluate data between $1.58\mu\text{m}$ and $1.68\mu\text{m}$. Figure 16 shows the results of applying this correction factor to itself. The values

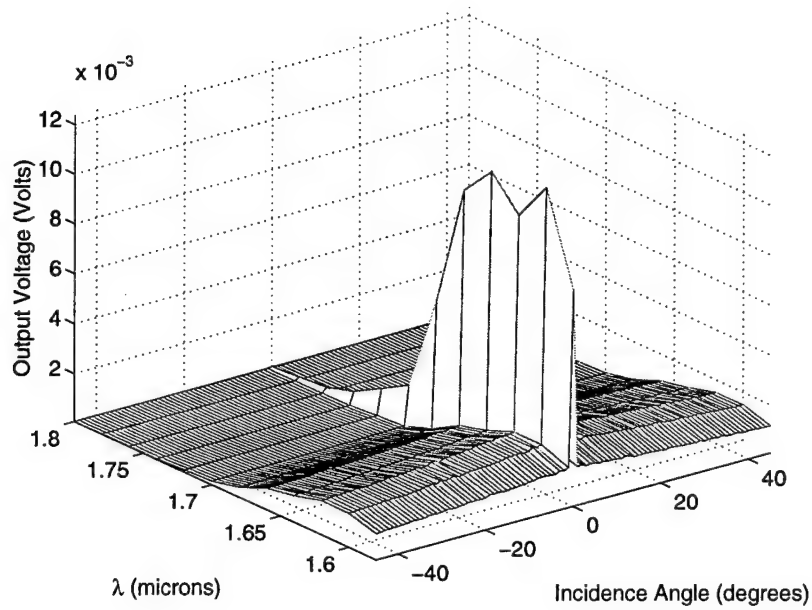


(a)

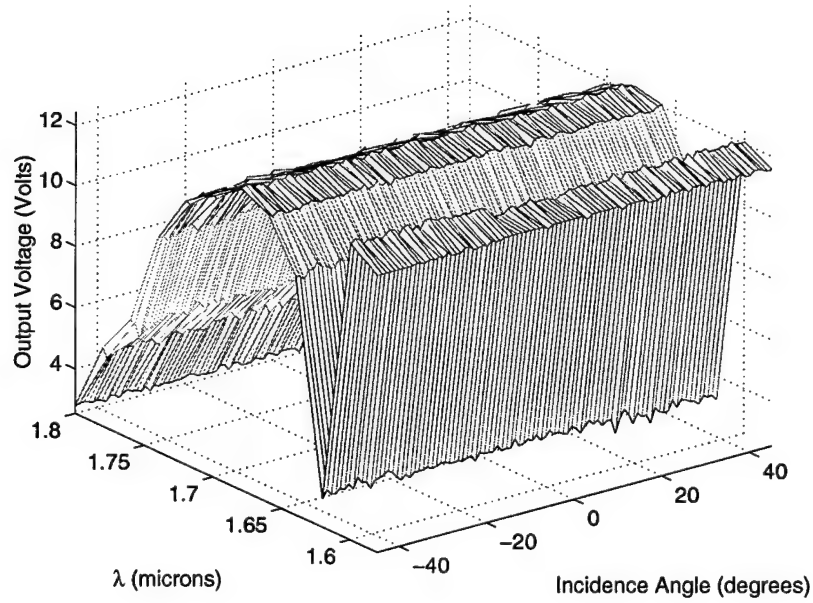


(b)

Figure 14 B-03 BRDF data using the absolute method of data analysis. (a) Mesh plot of BRDF data. Data points at one degree increments between -45 degrees and 45 degrees along the incidence angle axis. Data points at $0.02 \mu\text{m}$ intervals between $1.58 \mu\text{m}$ and $1.8 \mu\text{m}$ along the λ axis. (b) same BRDF data in semilog format to emphasize spacing of ρ' as a function of wavelength. The dashed lines represent the BRDF for a diffuse surface with 100%, 50% and 10% reflectance factor.



(a)



(b)

Figure 15 B-03 raw BRDF data. (a) Raw receiver signal voltage measured at one degree increments between -45 degrees and 45 degrees along the incidence angle axis and at $0.02\mu\text{m}$ intervals between $1.58\mu\text{m}$ and $1.8\mu\text{m}$ along λ axis. (b) Raw reference detector voltage measured concurrently with the signal voltage in (a).

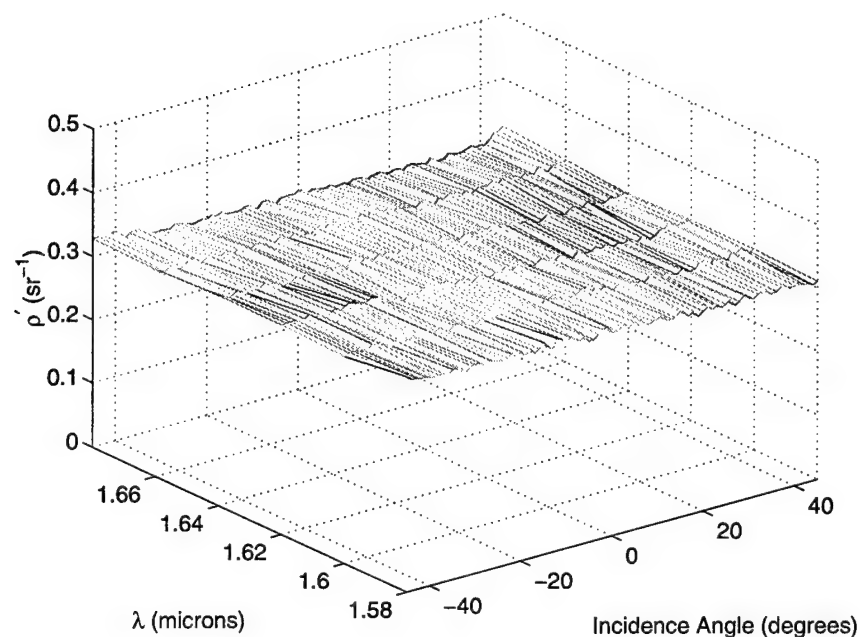
at each wavelength are now tightly bundled around $1/\pi$. The noise in the system causes the deviations from $1/\pi$ that is observed in the data. Had the raw data been noiseless, the RC method would have corrected all incident angles at each wavelength value to lie exactly on each other at $1/\pi$. Analysis of this data set does little more than illustrate the degree to which the data can be corrected.

The results obtained from the analysis of the second sample, B-03 are more interesting and provide some insight into the improvement of the data quality compared to that of the A-method analysis. To illustrate this fact, compare the RC method analysis results of Figure 17 to that of the A-method analysis results shown in Figure 14. The magnitude of the BRDF curves at each wavelength are approximately the same using the RC method while they vary about an order of magnitude in the results obtained using the A-method.

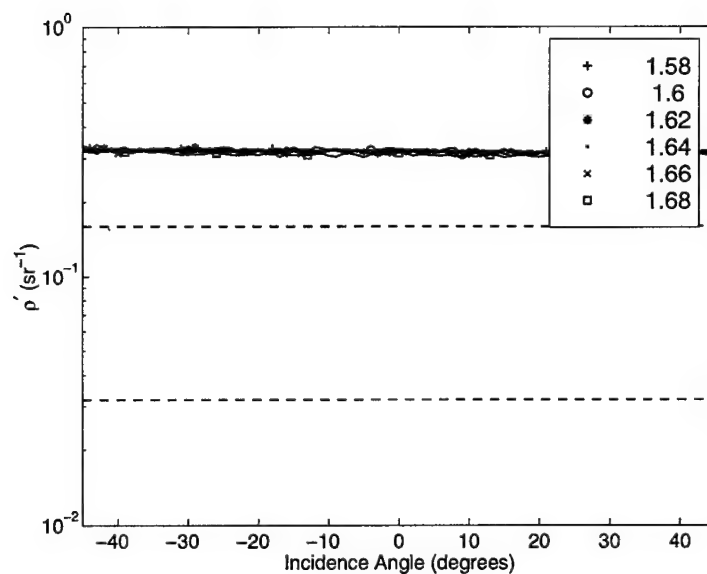
From this analysis method, these general comments can be made about the reflectance properties of this sample. First, it has a strong specular reflectance component at near normal incidence. However, once away from normal incidence, the sample acts as a diffuse reflector with a reflectance factor of approximately 20%.

The RC method of data analysis provides somewhat more information than the A-method does. Although the magnitude of the specular peaks may be suspect due to the method of calibration, the computed BRDF magnitudes from partially diffuse reflectors are approximately what is expected and in the author's opinion provide a general feel for the reflectance factor of a sample. One must be careful, however, in making any distinction in the reflectance factor from one wavelength to the next. In only one sample (which is discussed with the full set of BRDF data) was there any indication of a change in reflectance properties across wavelengths.

Due to problems that existed in the initial monostatic BRDF measurement system experimental setup, the acquired data did not achieve the level of accuracy and confidence necessary to produce a database of material BRDFs. In the next chapter, another system will be presented which builds on some lessons learned during the initial experiment and results in an improved BRDF measurement system which will produce the high level results necessary to build a database of material BRDFs.

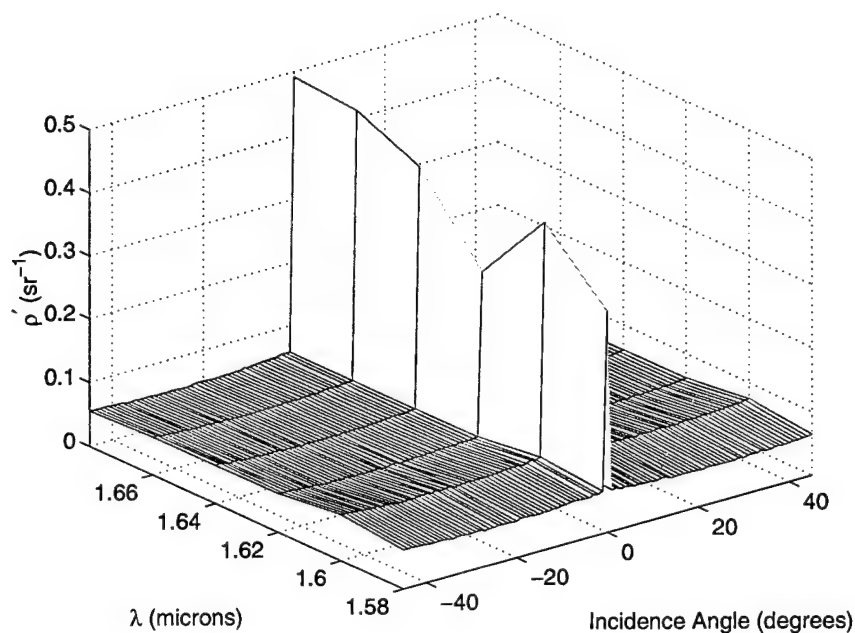


(a)

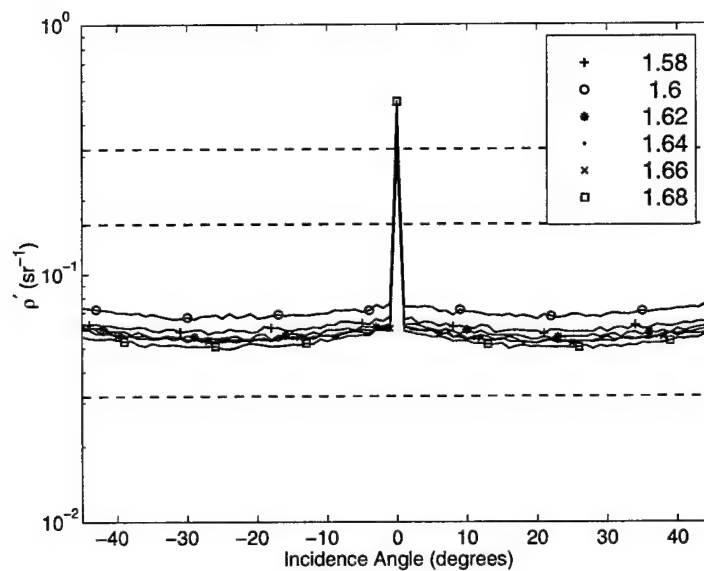


(b)

Figure 16 SRS-99-010 BRDF data using the Relative Calibration method of data analysis. (a) Meshplot of BRDF data. Data points are taken at one degree increments between -45 degrees and 45 degrees along the angle of incidence axis. Data points are taken at $0.02\mu\text{m}$ increments between $1.58\mu\text{m}$ and $1.68\mu\text{m}$ along the λ axis. (b) same BRDF data as (a) in semilog format to emphasize the magnitude of ρ' as a function of wavelength. The dashed lines represent the BRDF for a diffuse surface with 100%, 50% and 10% reflectance factor.



(a)



(b)

Figure 17 B-03 BRDF data using the Relative Calibration method of data analysis. (a) Meshplot of BRDF data. Data points are taken at one degree increments between -45 degrees and 45 degrees along the angle of incidence axis. Data points are taken at $0.02\mu\text{m}$ increments between $1.58\mu\text{m}$ and $1.68\mu\text{m}$ along the λ axis. (b) same BRDF data as (a) in semilog format to emphasize the magnitude of ρ' as a function of wavelength. The dashed lines represent the BRDF for a diffuse surface with 100%, 50% and 10% reflectance factor.

IV. Optimized Monostatic BRDF Experiment

4.1 Overview

This chapter presents an improved monostatic BRDF measurement system based on the experimental system described in Chapter III. A series of changes have been made, both in actual hardware and procedural, to the original system. These changes will improve the system performance to the point that high quality, repeatable results can be obtained from it.

4.2 Experiment Design

Figure 18 shows the experimental setup for the re-designed monostatic BRDF measurement system. The first step in improving the design of an existing system is to analyze the system that is in place and look for components or procedures that can be improved upon. The new system design is the result of such an analysis and the new components and procedures are implemented to correct the error sources observed in the original BRDF measurement system. A short discussion of each of the changes made to the system follows.

The output of the tunable laser source used in the original experiment was configured such that it produced a signal beam of $1.58\mu\text{m} - 1.80\mu\text{m}$ and an idler beam of $2.6\mu\text{m} - 3.26\mu\text{m}$. This laser was originally designed to include a full set of PPLN crystals to cover the full $1.5\mu\text{m} - 5.0\mu\text{m}$ range. However, at the time of the experiment, only a single crystal had been delivered and thus the limited wavelength range for the original experiment. Therefore, to achieve the full $1.5\mu\text{m} - 5.0\mu\text{m}$ wavelength range, the full set of PPLN crystals would be necessary.

Operation of the system over the full $1.5\mu\text{m} - 5.0\mu\text{m}$ range forces a change in the focussing optics used in the system. Because of high absorption levels above $2\mu\text{m}$, the beam expander and detector lenses have been replaced with off-axis parabolic aluminum mirrors. Aluminum mirrors have also been used in place of the glass turning mirrors of the original system.

The next optic that needs to be replaced is the pellicle beamsplitter. The purpose of this optic is to pick off a small portion of the beam for use as a reference signal to

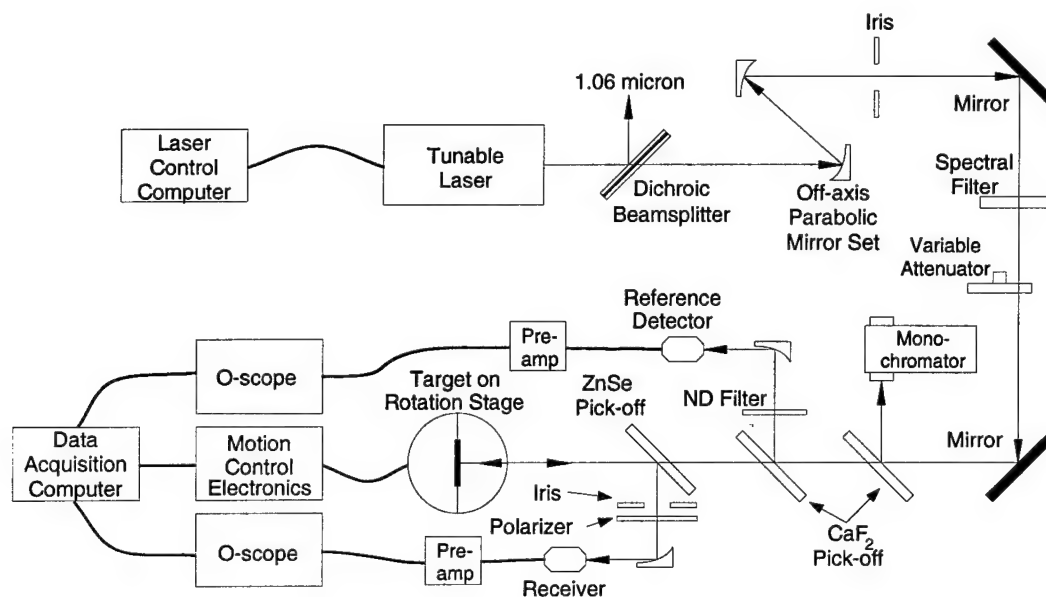


Figure 18 Revised monostatic BRDF measurement system

determine the power output of the laser. There are three main properties that this optic must have to accomplish this task. First, it must have a flat spectral response over the full wavelength range. Second, it must have a low reflectance factor, 5% – 10% would be ideal. Finally, it must be transparent between $1.5\mu\text{m}$ and $5.0\mu\text{m}$.

The optic chosen to do this is an uncoated calcium fluoride (CaF_2) window. Calcium fluoride has the proper index of refraction ($n \simeq 1.42$) to use Fresnel reflection to obtain the required reflectance factor. Also, the index changes only slightly over the wavelength range of interest and so provides a relatively flat spectral response(3). Since the laser is *s*-polarized, the important Fresnel reflection term is the *s*-polarized component. Figure 19 shows the Fresnel reflectance of a calcium fluoride window placed at 45° to the beam path. As can be observed from this figure, the calcium fluoride window meets the first two specifications for this optic. Calcium fluoride is essentially transparent at these wavelengths(8) and thus is an excellent optic to be used for the reference pick-off.

The second component in the system that needs replacement is the InGaAs detectors. These detectors do not provide full coverage of the wavelength range in the experiment. Replacing them with Indium Antimonide (InSb) photodiodes extends the wavelength range of the system to that of the laser. EG&G Optoelectronics produces a 77°K cooled InSb pho-

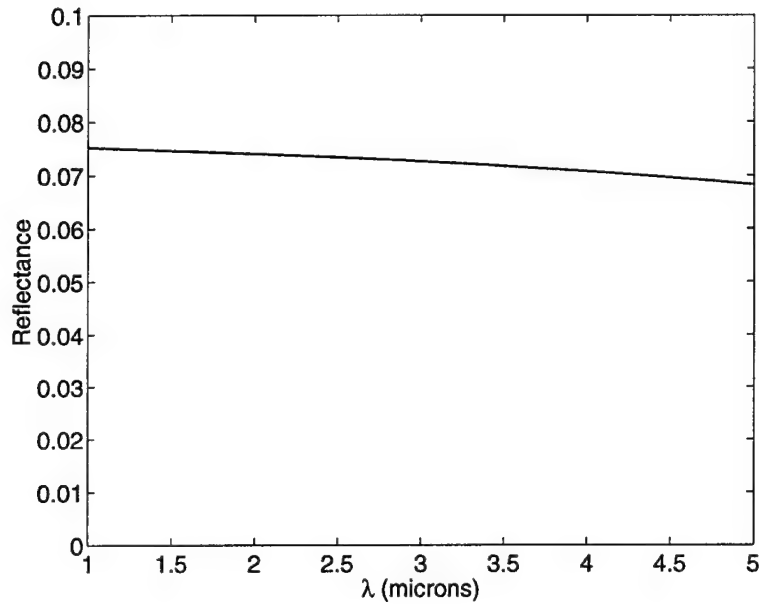


Figure 19 Single surface, *s*-polarized Fresnel reflectance from a calcium fluoride window at 45° incidence. Reflectance values are based on experimental index of refraction measurements.(3)

todiode that is designed for the 1.0 μ m to 5.5 μ m wavelength range. The J10D-M204-R500U model provides a 0.5mm diameter active area with a responsivity of 3 A/W that can operate at the 20kHz pulse repetition rate. This detector meets the specified wavelength range, bandwidth and active area requirements of the system.

The output from both InSb photodiodes are routed to preamps and on to oscilloscopes where a number of laser pulses will be averaged to improve the signal to noise ratio. The electronics will be kept the same in each channel for this design as opposed to the previous design where the reference channel was routed through an oscilloscope and the receiver channel through a lock-in amplifier. This should also boost system performance.

Although not a large problem in the previous setup, the broadband beamsplitter will also be replaced with an uncoated optic with a flat spectral response over a wide wavelength range. The optic selected to replace it is a zinc selenide window. Figure 20 shows the *s* and *p*-polarized Fresnel reflectances of a zinc selenide window placed at 45° in the beam path. An ideal window would have a 50/50 split in the transmitted and reflected powers to provide maximum signal to the receiver. However, the 70/30 split of the zinc selenide

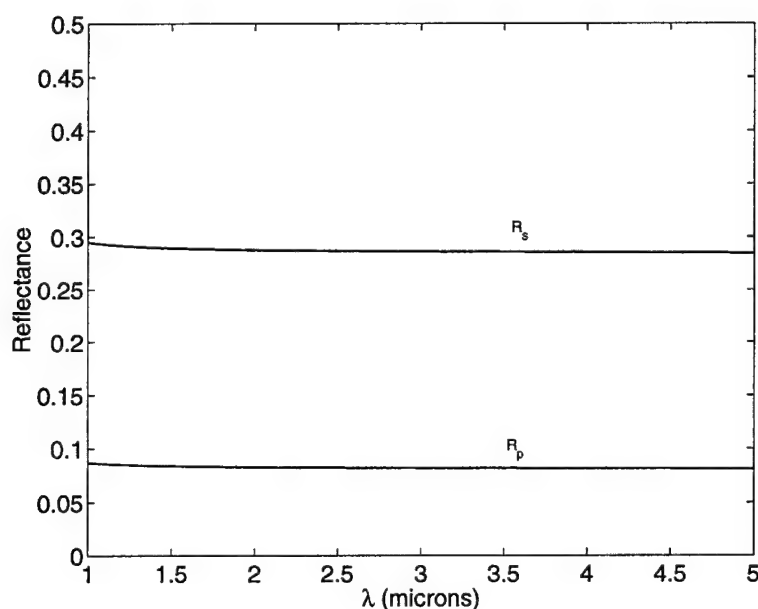


Figure 20 Single surface Fresnel reflectance of s and p polarization components from a zinc selenide window at 45° incidence. Reflectance values are based on experimental index of refraction measurements.(3)

window provides the necessary performance for the system while maintaining uncoated optics.

Another possible replacement for the broadband beamsplitter is an apertured mirror. A 5mm hole drilled at 45° through the center of an aluminum mirror adds many benefits to the system. First, 100% of the power transmitted through the second calcium fluoride pick-off window will be incident on the sample. Second, close to 100% of the power reflected back to the mirror from the sample will be reflected into the receiver with no preference given to a certain polarization. The one drawback of using such a mirror is that there is a 5mm diameter hole in the center. Some of the power reflected from the sample will travel back through this hole and never be measured by the receiver. For a diffuse reflector and the same receiver solid angle as the original experiment, only 1.3% of the power is lost through this hole. Obviously, this is the best case scenario. As the sample becomes more specular in its reflectance properties, a higher percentage of the power is lost through the hole and for a purely specular reflector, 100% of the power will travel back through the hole when the sample is at normal incidence. Even with this complication, an apertured

mirror could prove to be an excellent method for increasing the power collected at the receiver for both polarizations.

Some new components need to be included to further improve the system. First a neutral density filter is added to the beam path between the reference detector pick-off and the reference detector. The purpose of this filter is to ensure that the reference detector stays in a linear operating region. It is a requirement that this filter be spectrally calibrated to allow an accurate measurement of the beam power reflected by the receiver pick-off window.

A variable attenuator is also added to the beam path between the two turning mirrors. This will be used to reduce the incident beam power to prevent saturation of the receiver for samples with a strong specular component. It is not necessary that the variable attenuator be spectrally calibrated since it is in the beam path before the reference detector pick-off. However, a flat response is still desired to keep the signal levels constant.

A spectral filter is also added to the system between the two turning mirrors. The spectral filter is needed so that only one of either the signal or the idler beam is passed at a time. This was not a problem in the original experiment because the InGaAs detectors could not see the idler beam at $2.6\mu\text{m}$. But the InSb detectors specified in this system have good response over the full range so the experiment must be designed to look at only one of the output wavelengths at a time.

One problem with the initial BRDF measurement system setup was that there was no way of knowing exactly what wavelength the laser was operating at. That problem will be fixed in this system with the addition of a scanning monochromator. An uncoated calcium fluoride optic will be used to pick off about 6% of the beam for input into the monochromator. The monochromator can then be scanned during the sample rotation scan to determine the laser wavelength and linewidth.

The final addition made to the experiment is a rotatable polarizer placed between the ZnSe window and the receiver. With the polarizer in place, a data set can be taken at both the *s* and the *p*-polarization setting. This polarizer will remove the ambiguity as to which reflectance factor to use in the data reduction algorithms when measuring non-specular

reflecting samples. It will also add information about the polarization properties of the sample. For example, does the light reflected from the sample tend to be polarized the same as the input, rotated from the input, or does the sample act to de-polarize the reflected light?

Even with the new hardware in place, there are still a couple of procedural steps that can be taken to further improve the quality of the data. First, the pick-off optic calibrations need to be done in the system using the same source as in the experiment. By doing this, the calibration and experimental conditions are the same and there is no error due to changes in alignment or differences in the rotation of the optics.

Once the optics in the path are calibrated, the overall system can be calibrated using known reflectance standards. During the original BRDF measurements, diffuse reflectance standards were used to both calibrate and test the system. This needs to be repeated again for this system. A calibrated specular reflector also needs to be obtained for calibration and testing of the system for specularly reflecting samples. This is a necessary step to place confidence in the measurement of non-diffuse samples.

The data acquisition system also needs to be changed to allow averaging of several measurements. Currently, a single data point is taken at each interval. This produces noisy data with low statistical significance. A digital oscilloscope could be used for this function by taking several seconds worth of laser pulses and averaging the signal to obtain a statistically significant measurement.

Many improvements have been made to the original monostatic BRDF measurement system. Each one of these improvements was implemented to remove the sources of error observed in the original system. These improvements will undoubtedly result in better BRDF measurement results.

V. Conclusions and Recommendations

5.1 Conclusions

This research investigated two areas of great importance to active multispectral laser radar systems — band selection techniques and the measurement of the bidirectional reflectance distribution function. A new multispectral band selection technique is presented which uses a correlation-based method to select bands. This algorithm provides an intuitive feel for the band selection process by choosing bands much like a person would. This intuition was also realized in the classification process as the bands chosen by the CBand selection algorithm outperformed those picked by the FSS algorithm for the three band case.

A monostatic BRDF measurement system was also developed and tested on a series of samples of interest to the Air Force Research Laboratory. Based on these tests, an improved system design was developed to remove the sources of error observed with the first design. The results of this redesign will provide the necessary improvements to the system to obtain high quality, repeatable BRDF measurements.

5.2 Recommendations

Both of the areas researched in this thesis have the possibility for follow-on work. The CBand selection algorithm presented in this thesis could be improved by developing rules for selection of adjacent spectral bands. Currently, each of the first three bands selected by the CBand algorithm provides a great deal of spectral information about the material classes to the classifier. However, any bands selected after the third band has a high probability of being closely spaced to one of the previously selected bands (see Figure 6). When one of these closely spaced bands is added to the set, the classification rate shows no improvement because no new information is contained in this added band. The FSS algorithm suffers from the same problem, except that it shows up in the selection of the third band after the first band pair is chosen. An improvement could be made to the algorithm to determine a natural way to prevent these consecutive bands from being selected.

The obvious follow-up for the monostatic BRDF measurement system would be to integrate the recommendations from Chapter 4 into an improved system and test its performance. It is suggested that this experiment be constructed in a laboratory either at AFIT or AFRL as this is a large task that cannot be successfully completed in a couple of weeks.

Because of the high number of angles and wavelengths at which data needs to be collected, efficient acquisition of the data is also important. Although not part of the original task at hand, an automated data collection system is almost a necessity in a system such as this. It would be used to acquire data from the receiver and reference channels and also act as the automated control for the rotation stage. Some up-front work on this system will reduce the error introduced by human factors and in the long run result in a better set of BRDF measurements.

Another option for system improvement is to design and test a directional hemispherical reflectance (DHR) attachment. The bulk of the BRDF measurement system would stay the same with only the receiver and sample holder configurations changing. Design of such a system would provide the ability to measure the DHR across a continually tunable wavelength range of $1.5\mu\text{m} - 5.0\mu\text{m}$.

Once the BRDF and DHR measurement system is in place and fully operational, it could be used to build a database of high spectral resolution BRDF and DHR measurements for a wide range of material samples. Currently, samples of paint, cloth, and vegetation are of high importance to the Air Force.

Appendix A. BRDF Data Descriptions

This section contains the naming designation and data file contents used during this experiment. Consistent naming and file formats has allowed automated data reduction programs which has increased the speed and ease of producing the data in a format which is both consistent and easily produced.

A.1 File Names

Data files are named using two distinct parts. The first part is the sample designator and the second is the wavelength designator. The two parts of the filename are separated by an underscore (_) and a '.dat' extension is used. The only restriction in the construction of the data filename is that it must be legal for the operating system being used for data reduction.

For this research, the data filenames were determined based on the sample ID designator. Each set of measurements is placed into its own directory named by its sample ID name. For example, the data collected for sample B-03 at $1.58\mu\text{m}$ is located in the directory *B03* and is saved under the filename *b03_158.dat*.

A.2 Data File Format

Each data file has a format that must be adhered to for the data analysis algorithms to work properly. A simple description of each of these formats is now presented.

The BRDF measurement data files consist of three columns of data. The first column is a zero-based counter that increments for each new data point. The second column is the raw signal value from the receiver channel and the third column is the raw signal value from the reference channel.

The calibration data files are in a different format. They begin with nine lines of header information which give the instrumental setup including the start and stop wavelengths, the step size, and the number of averages used in the calibration process. Line 10 starts the actual data which consists of two columns, the first is the signal level

Table 2 Description of sample IDs used during the BRDF measurement experiment.

<i>Sample ID</i>	<i>Vehicle</i>	<i>Description</i>
SRS-99-010		Diffuse reflectance standard with 99% reflectance factor
SRS-50-010		Diffuse reflectance standard with 50% reflectance factor
B-02	2S1	Large single paint chip
B-03	2S1	Large thick paint chip (color difference from B-02)
D-08	SA-8	Large single green paint chip
E-38	GAZ-66	Three long overlapping flecks of green paint
GCP		Green CARC paint sample on aluminum

and the second is the standard deviation of the signal level based on the number of averages used to compute the signal level.

The spectral response files are generated based on the calibration data and consist of two columns. The first column consists of a series of wavelengths that define the range of the spectral response curves. The second is the value of the curve at its wavelength.

A.2.1 BRDF Data Files. Table 2 correlates the sample IDs with their respective vehicle, when applicable. It also contains a brief description of the sample when that information is known.

A.2.2 Component Calibration and Response Curves. This section contains the experimental setup used in the calibration of the beamsplitters and the measurement of the detector response. The spectral response curves for each component are given following the description of the experimental setup.

Figure 21 shows the experimental setup used to measure the beamsplitter spectral response curves. The setup includes a triple grating monochromator, chopper wheel, a pair of lenses and a detector. The beamsplitter under test is placed between the two lenses. A white light source is used as an input to the monochromator. From it, the monochromator produces a monochromatic output which is scanned from $1.2\mu\text{m} - 1.8\mu\text{m}$. The output of the monochromator is chopped at 140 Hz, passed through the first lens, the beamsplitter, and focused on the detector by the second lens. Two data collection runs were completed, one with the beam splitter in place and the other with it removed. The ratio of the

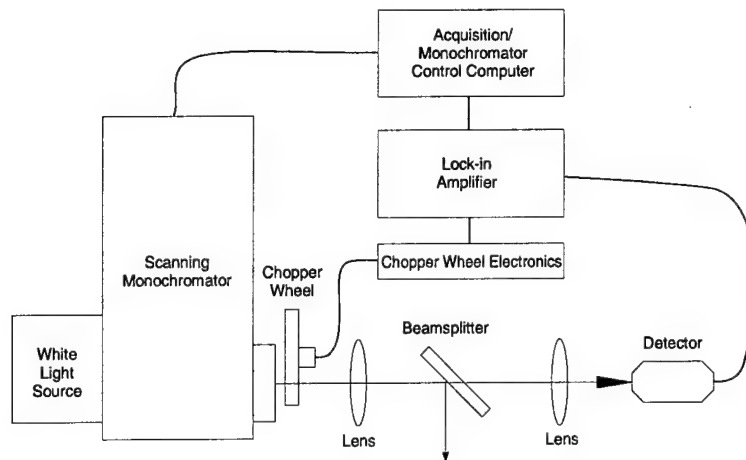


Figure 21 Laboratory setup for beamsplitter calibration.

'beamsplitter in' collection to the 'beamsplitter out' collection is the transmission of the tested beamsplitter.

The normalized detector response was measured using a setup similar to that used in the beamsplitter calibration. Figure 22 shows the layout for the normalized detector response measurement. Again, two data collections are completed, one with a detector with a flat spectral response and the other with the InGaAs APD detector used in the BRDF measurement experiment. The ratio of the InGaAs APD output to the reference detector provides the relative response of the two detectors. Since the reference detector has a flat spectral response, normalization of this ratio gives the normalized spectral response of the InGaAs detectors shown in Figure 25.

Figure 23, Figure 24 and Figure 25 give the spectral response of the pellicle beamsplitter, broadband beamsplitter and the normalized detector response, respectively.

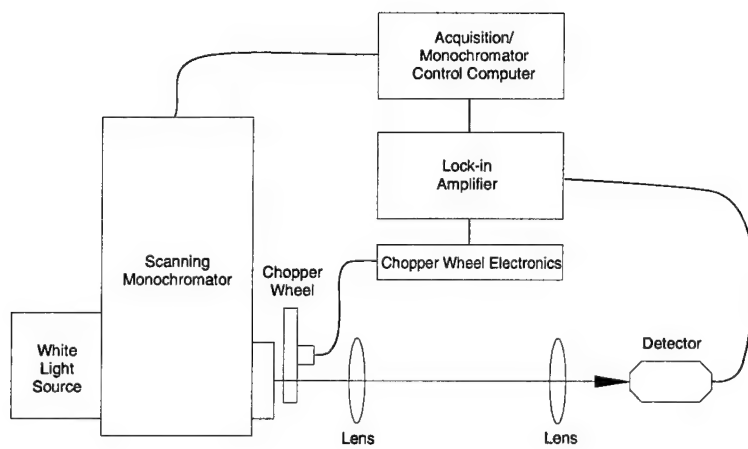
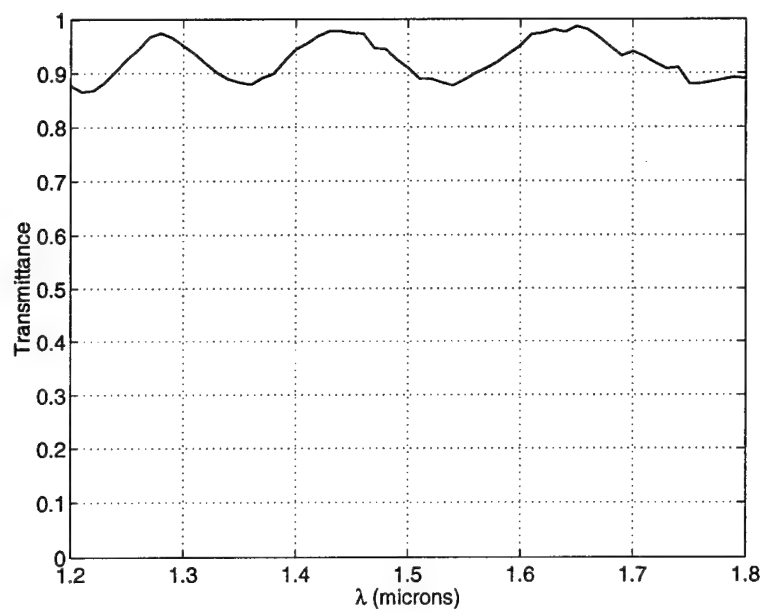
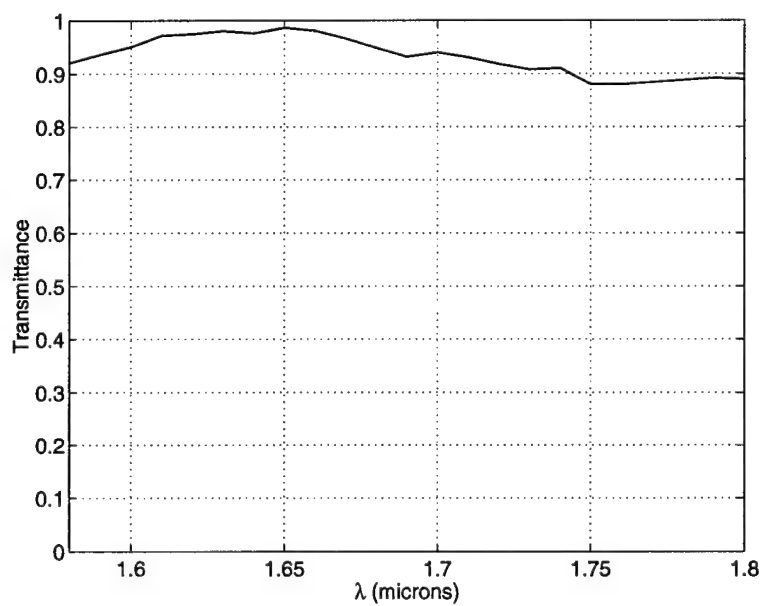


Figure 22 Laboratory setup for detector calibration.

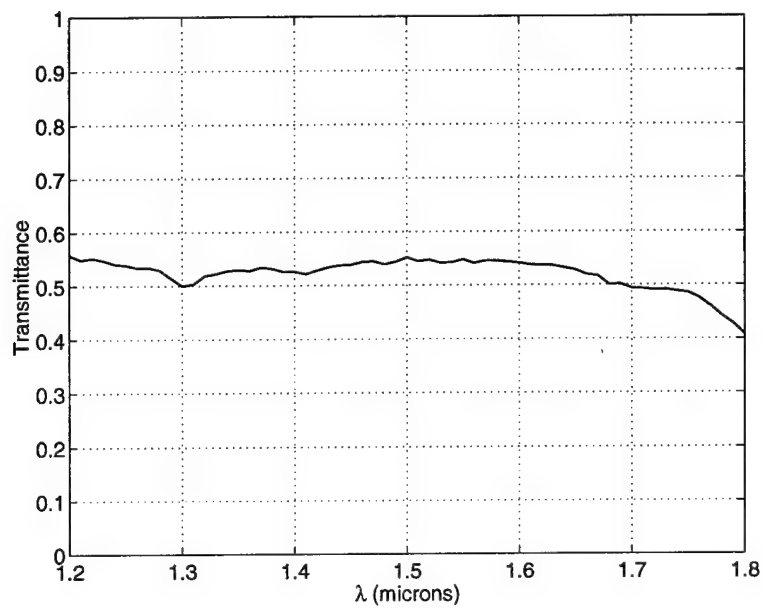


(a)

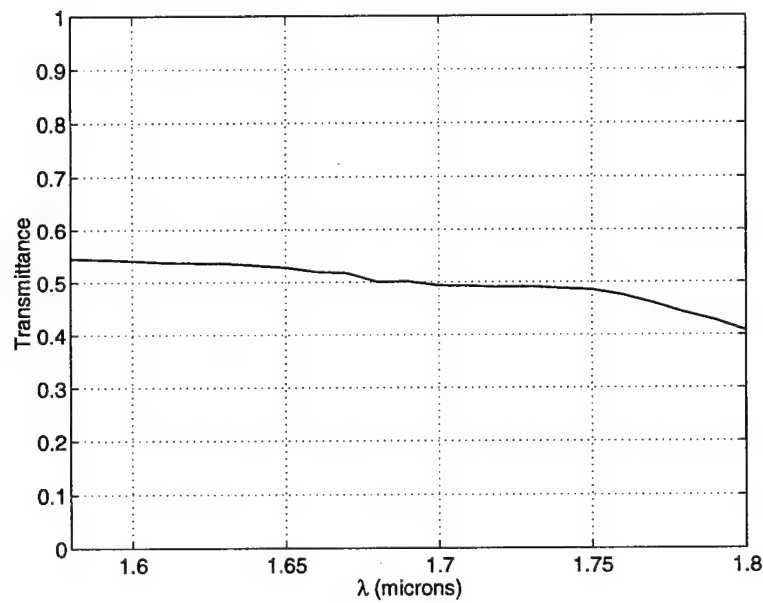


(b)

Figure 23 Pellicle beamsplitter spectral response curves. (a) Data over full calibration range. (b) Data over BRDF experiment range.

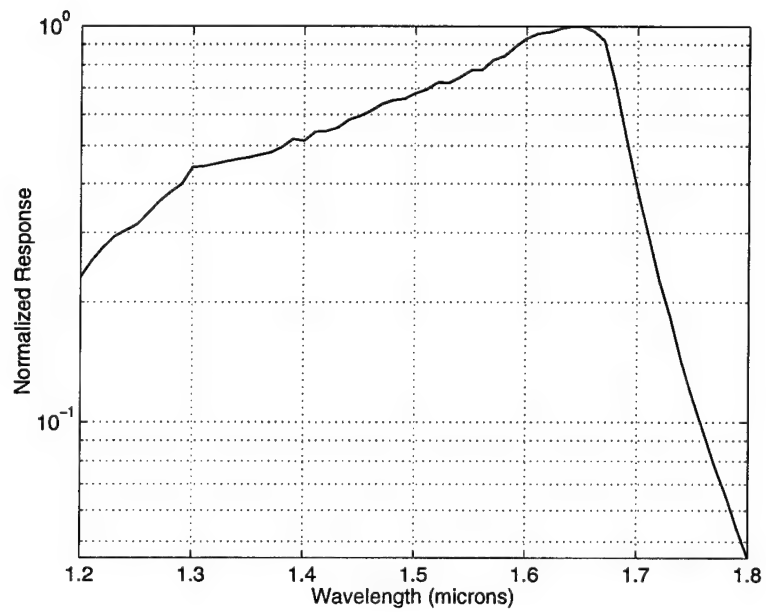


(a)

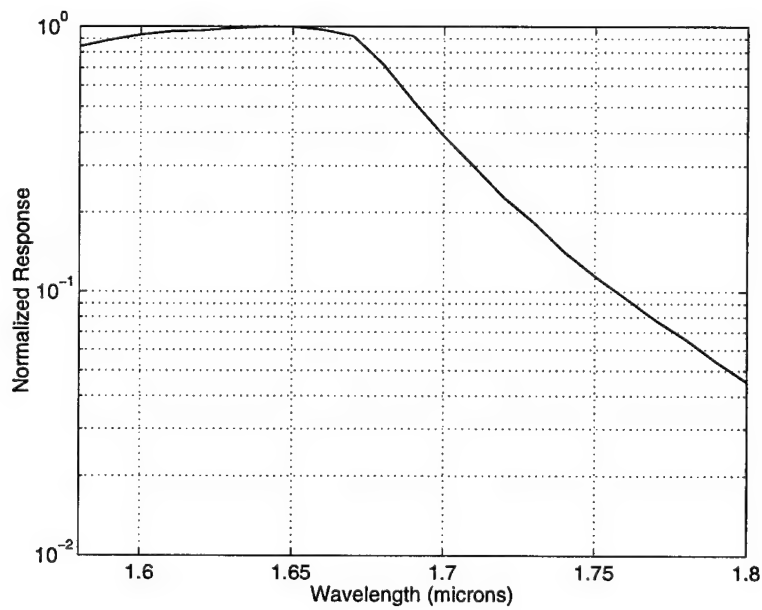


(b)

Figure 24 Broadband beamsplitter spectral response curves. (a) Data over full calibration range. (b) Data over BRDF experiment range.



(a)



(b)

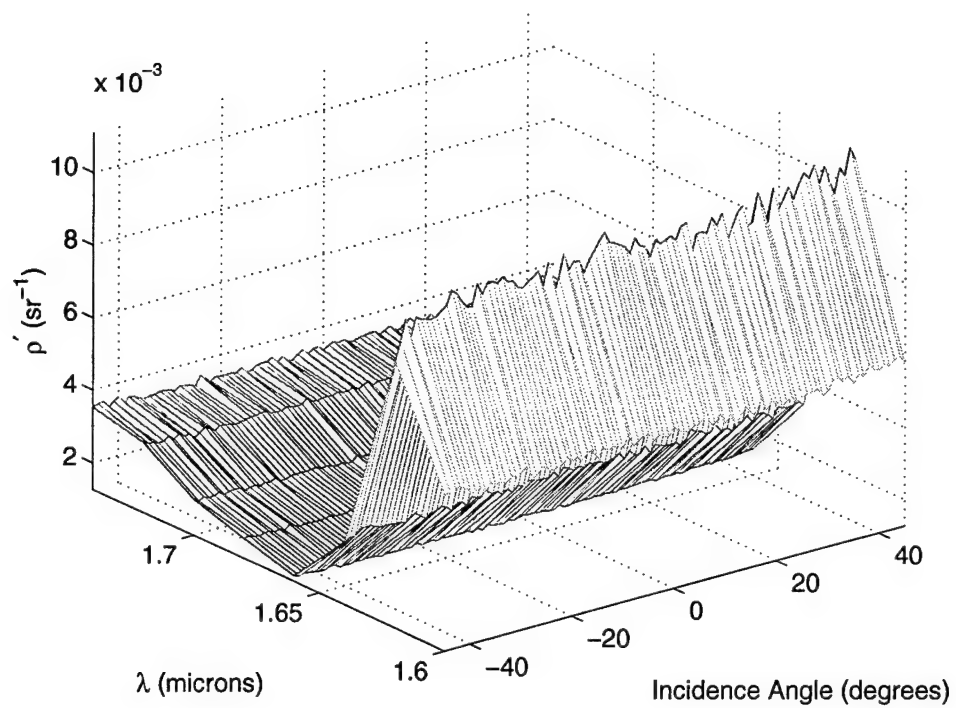
Figure 25 InGaAs detector normalized spectral response curves. (a) Data over full calibration range. (b) Data over BRDF experiment range.

Appendix B. BRDF Data

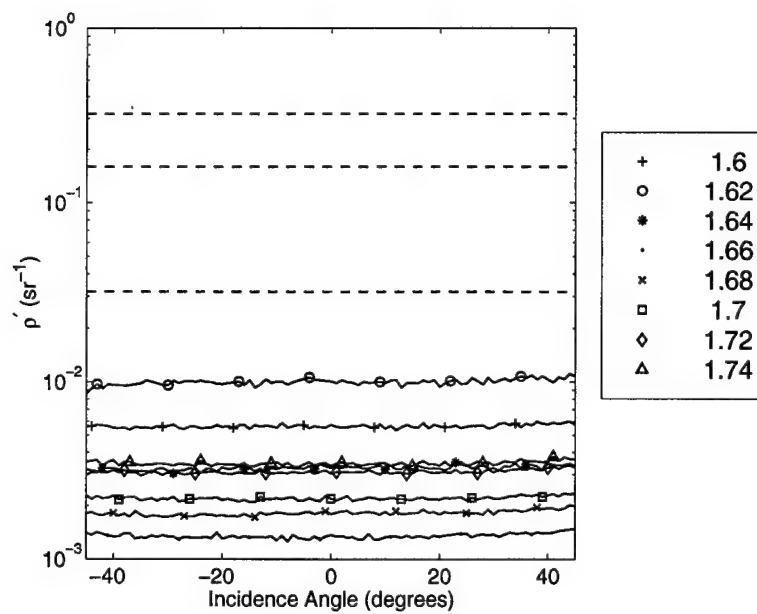
B.1 Absolute Method Results

This section contains a full set of results for the A-method of data reduction. These include Figure 26 to Figure B.1.

For each of the samples, (a) is a meshplot of the BRDF data. The data points are taken at one degree increments between -45 degrees and 45 degrees along the angle of incidence axis and at $0.02\mu\text{m}$ increments between $1.58\mu\text{m}$ and $1.80\mu\text{m}$ along the λ axis. Occasionally, data dropouts may cause the data to begin after $1.58\mu\text{m}$ or end before $1.80\mu\text{m}$. (b) is the same BRDF data as in (a) but is in a semilog format to emphasize the magnitude of ρ' as a function of wavelength. The dashed lines in (b) represent the BRDF for a diffuse surface with 100%, 50% and 10% reflectance factor.

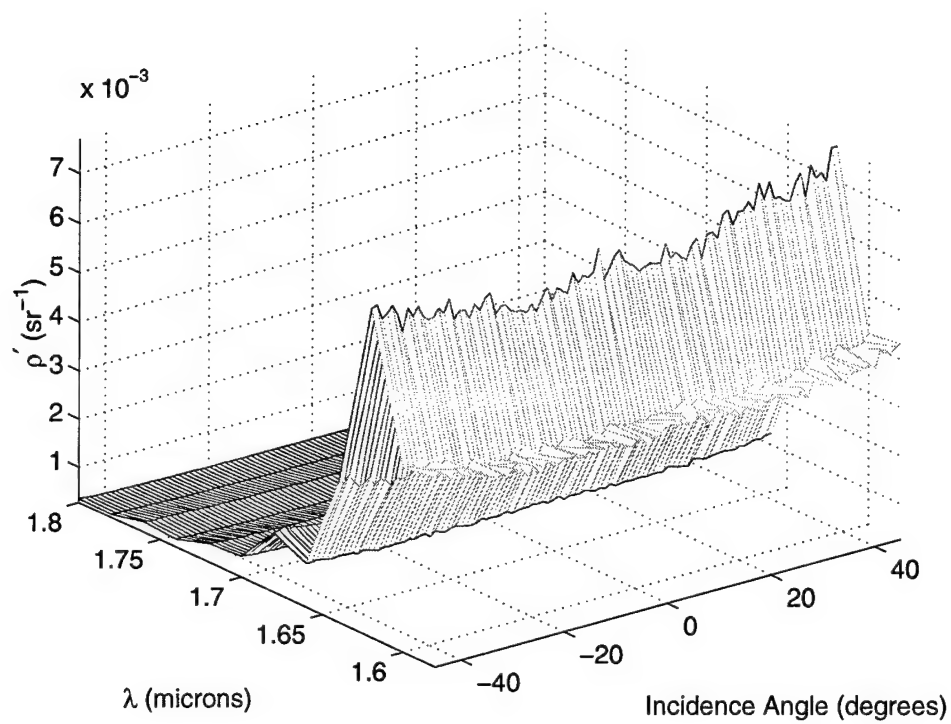


(a)

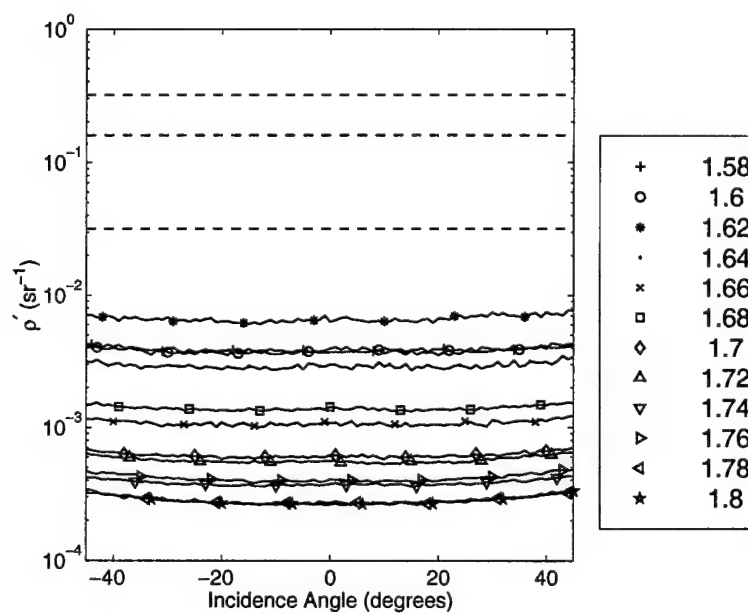


(b)

Figure 26 A-Method: SRS-50-010 BRDF data.

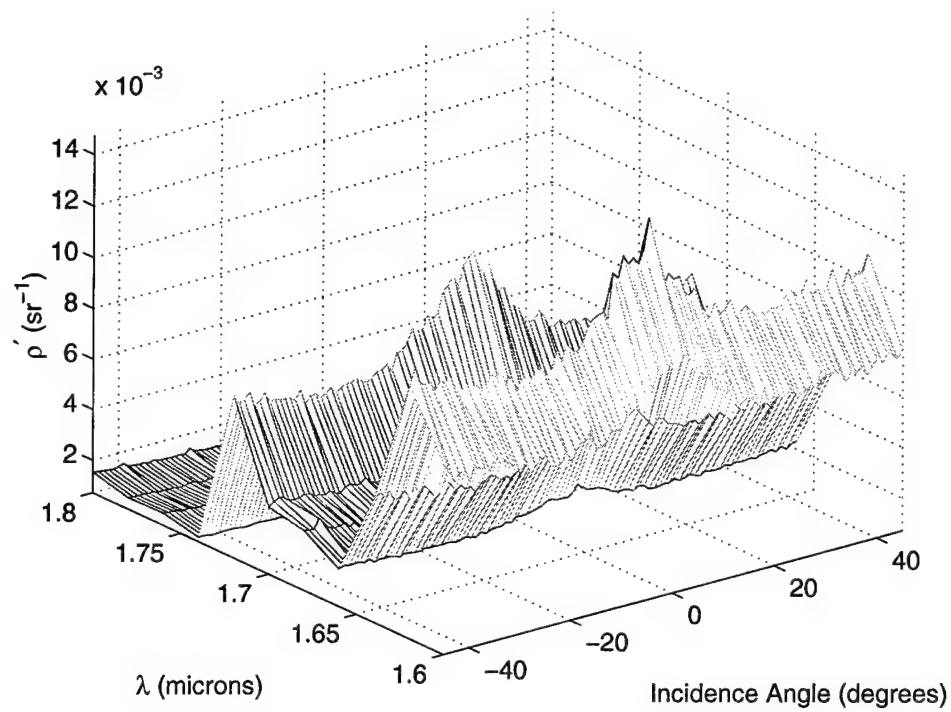


(a)

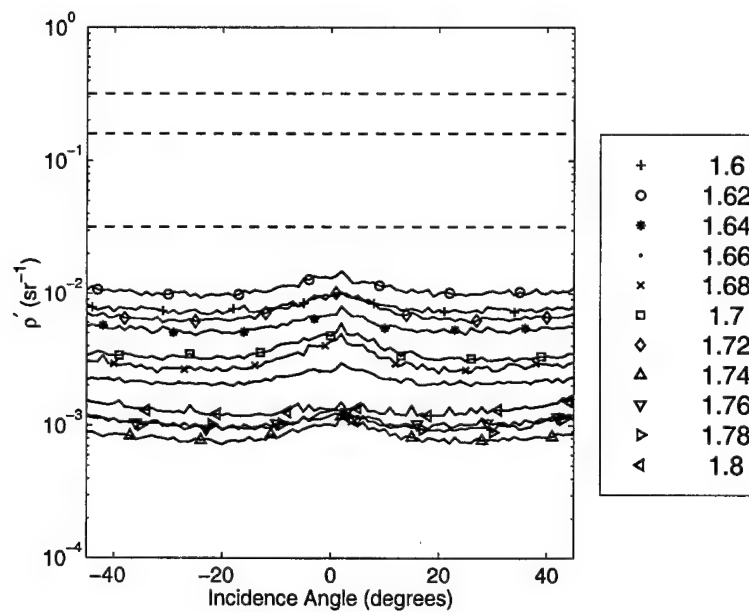


(b)

Figure 27 A-Method: Green CARC Paint BRDF data.

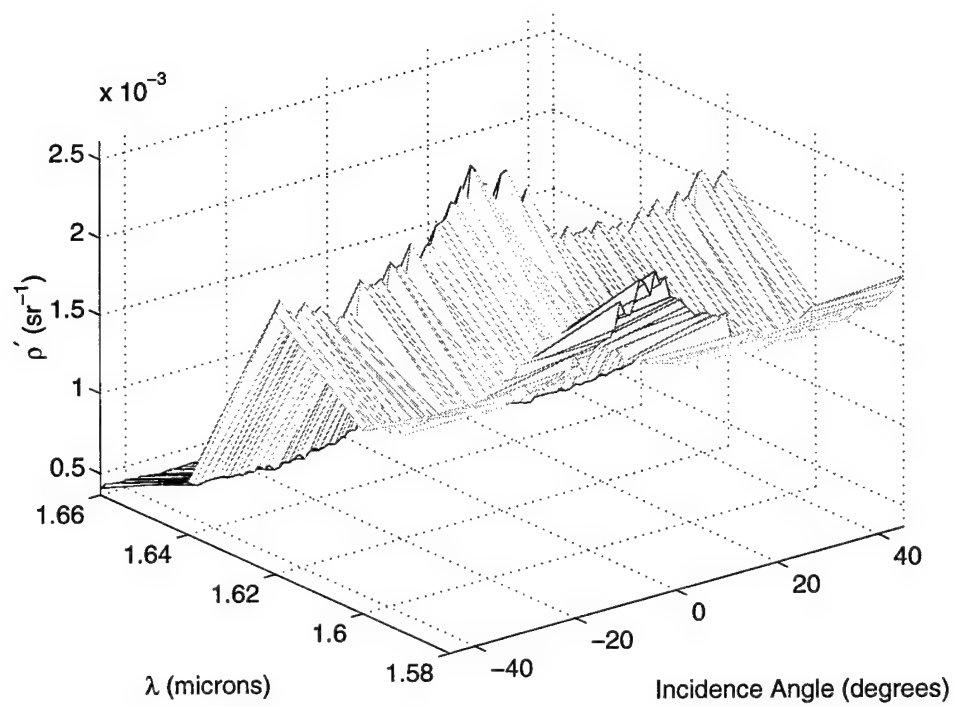


(a)

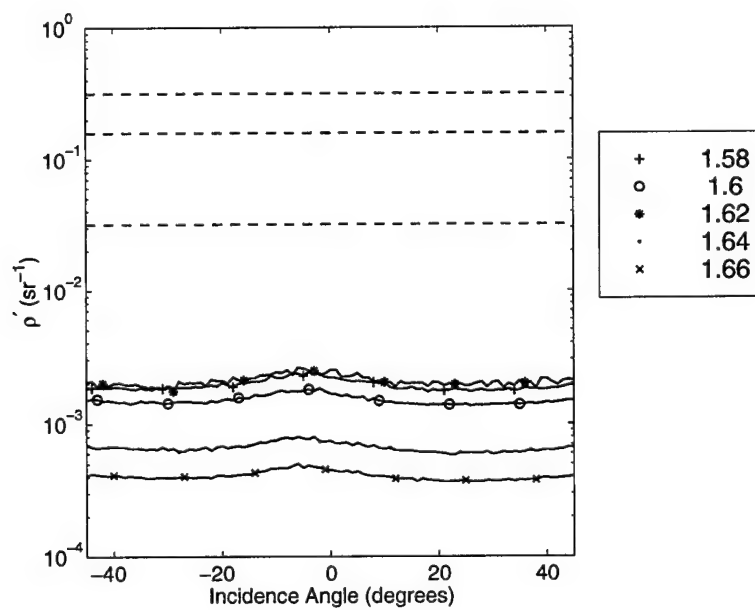


(b)

Figure 28 A-Method: B-02 BRDF data.

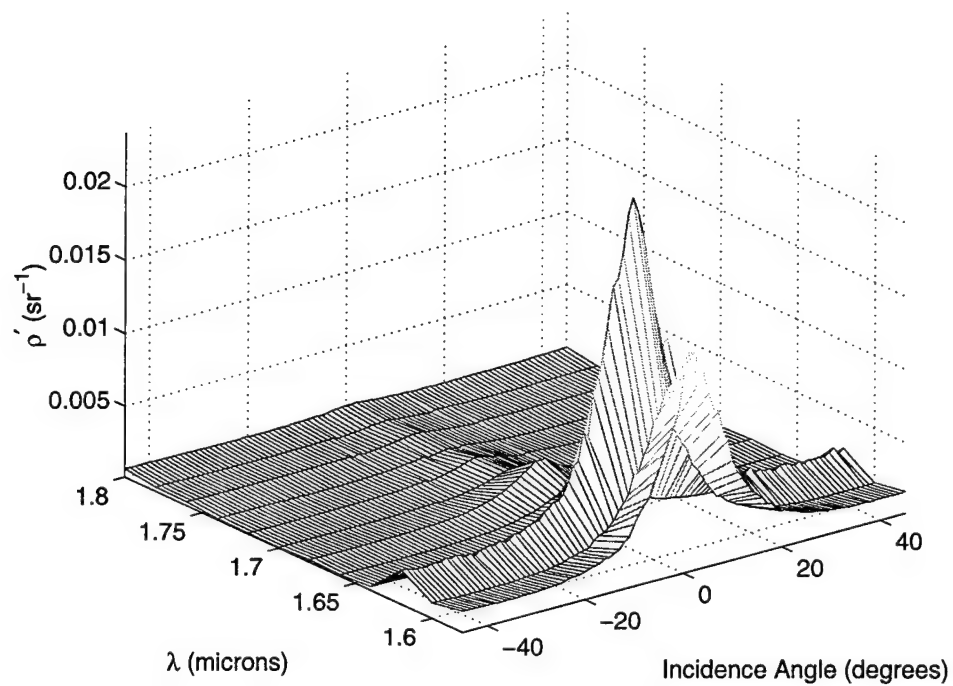


(a)

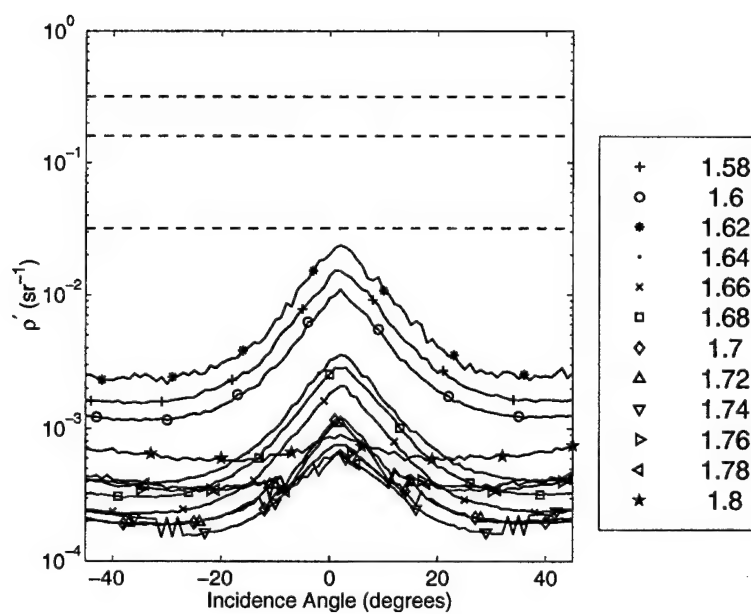


(b)

Figure 29 A-Method: D-08 BRDF data.



(a)



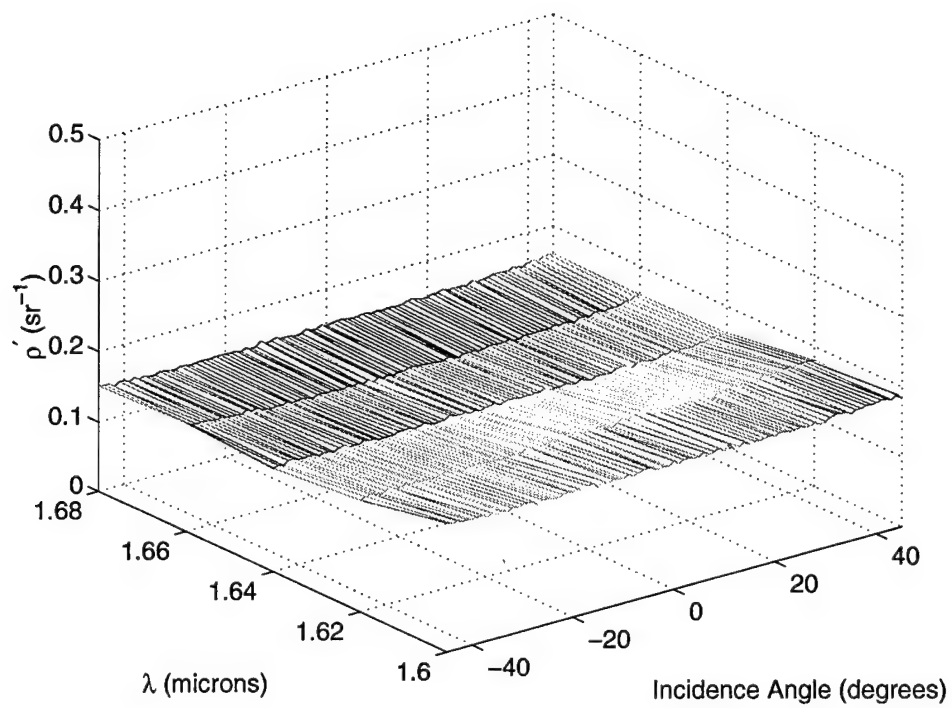
(b)

Figure 30 A-Method: E-38 BRDF data.

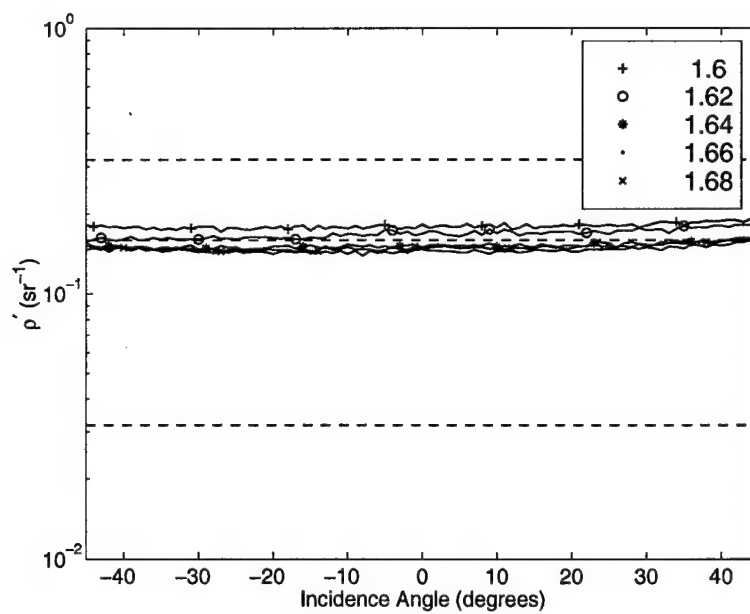
B.2 Relative Calibration Method Results

This section contains a full set of results for the A-method of data reduction. These include Figure B.2 to Figure B.2.

For each of the samples, (a) is a meshplot of the BRDF data. The data points are taken at one degree increments between -45 degrees and 45 degrees along the angle of incidence axis and at $0.02\mu\text{m}$ increments between $1.58\mu\text{m}$ and $1.68\mu\text{m}$ along the λ axis. Occasionally, data dropouts may cause the data to begin after $1.58\mu\text{m}$ or end before $1.68\mu\text{m}$. (b) is the same BRDF data as in (a) but is in a semilog format to emphasize the magnitude of ρ' as a function of wavelength. The dashed lines in (b) represent the BRDF for a diffuse surface with 100%, 50% and 10% reflectance factor.

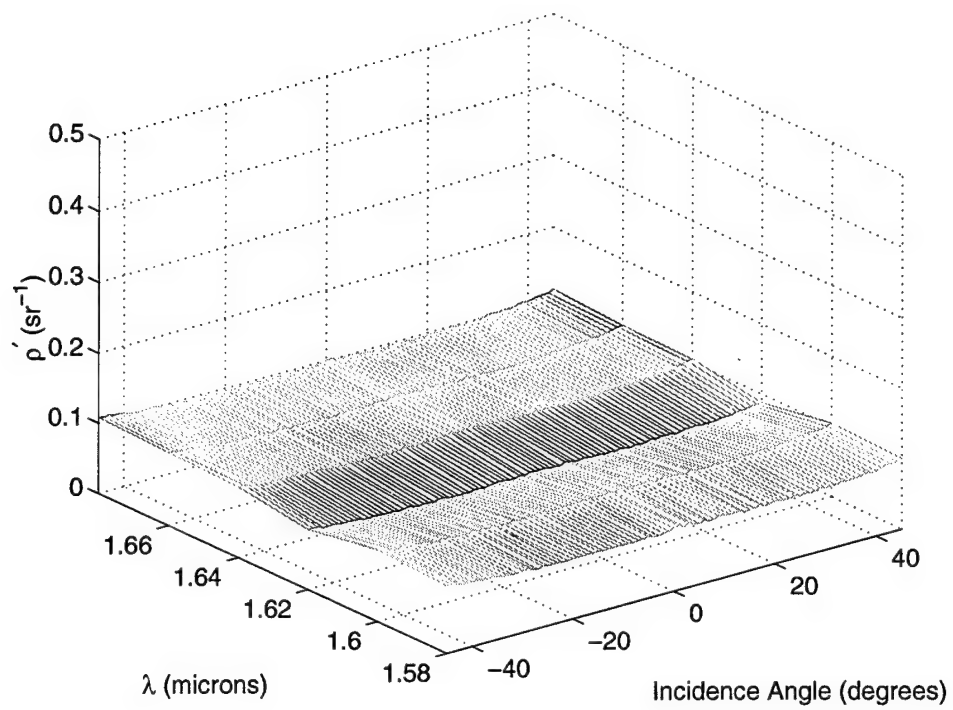


(a)

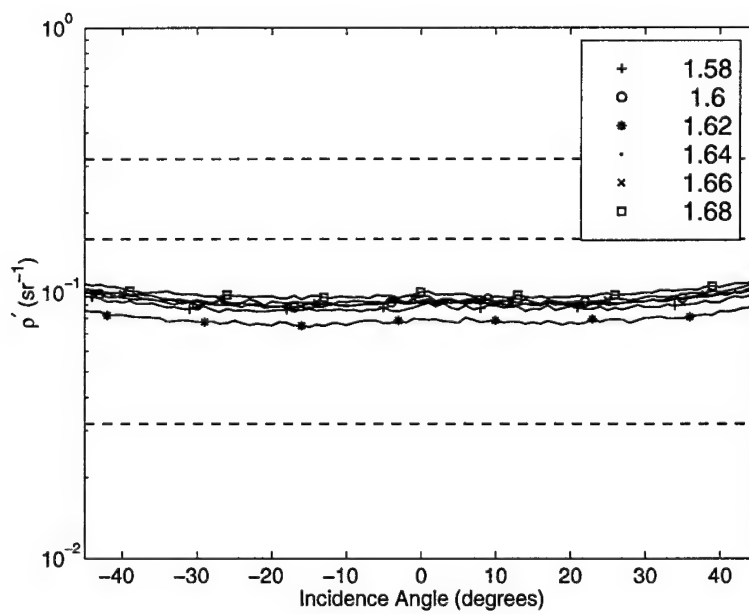


(b)

Figure 31 RC Method: SRS-50-010 BRDF data.

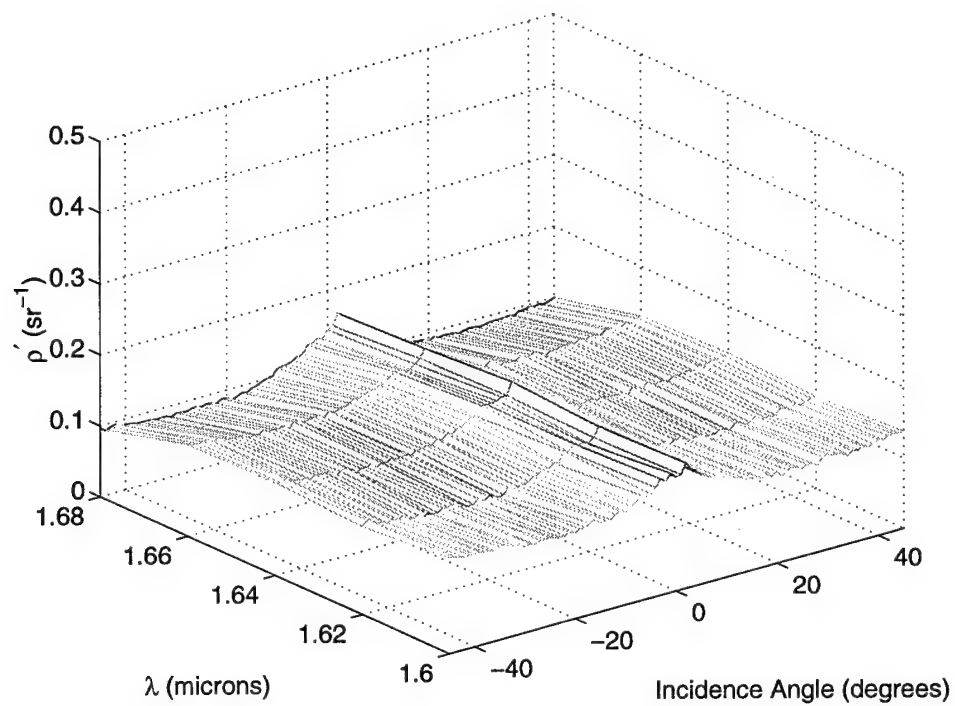


(a)

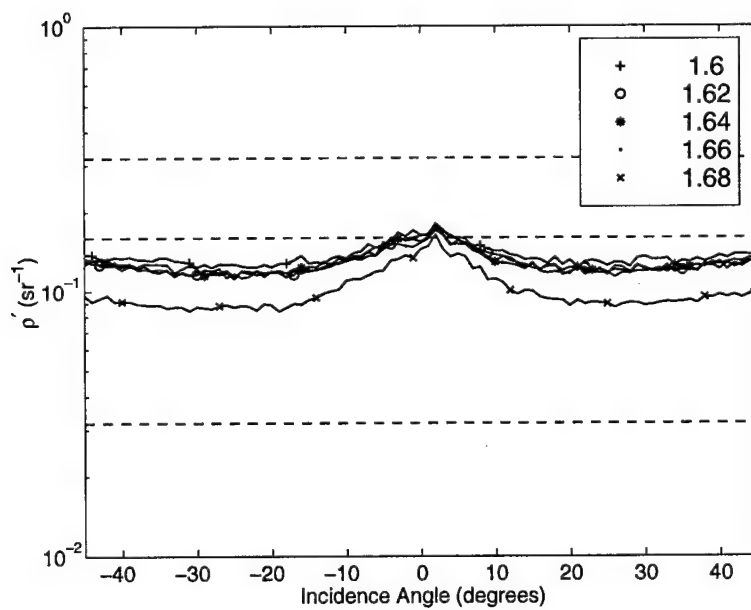


(b)

Figure 32 RC Method: Green CARC Paint BRDF data.

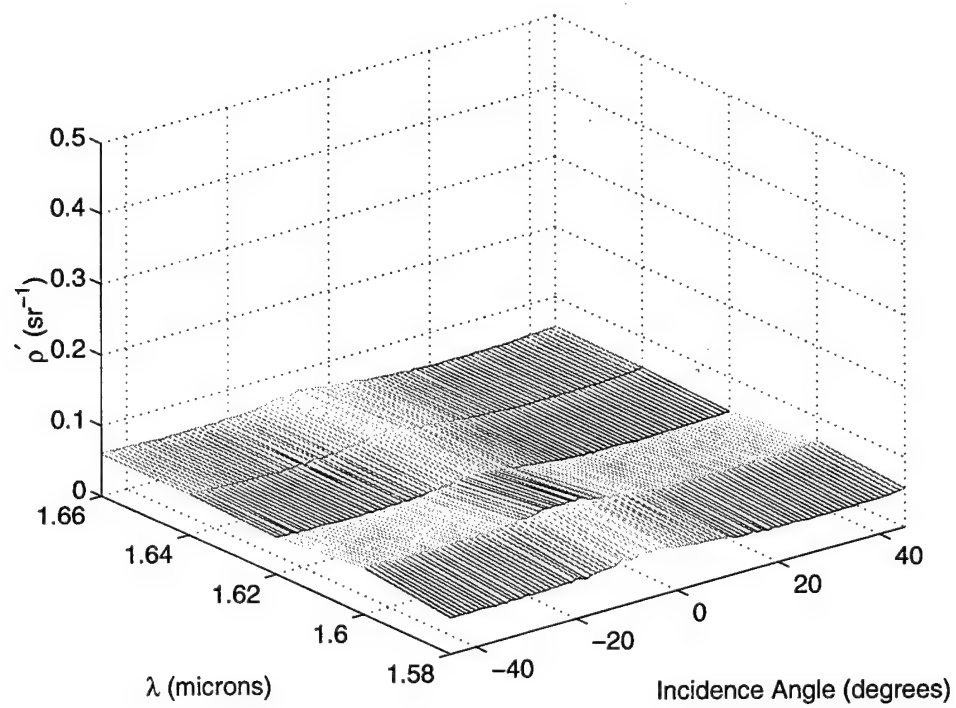


(a)

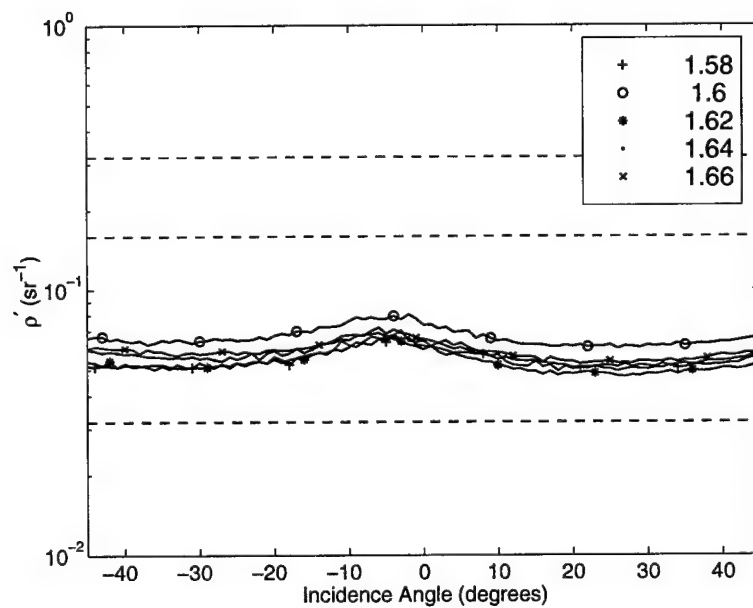


(b)

Figure 33 RC Method: B-02 BRDF data.

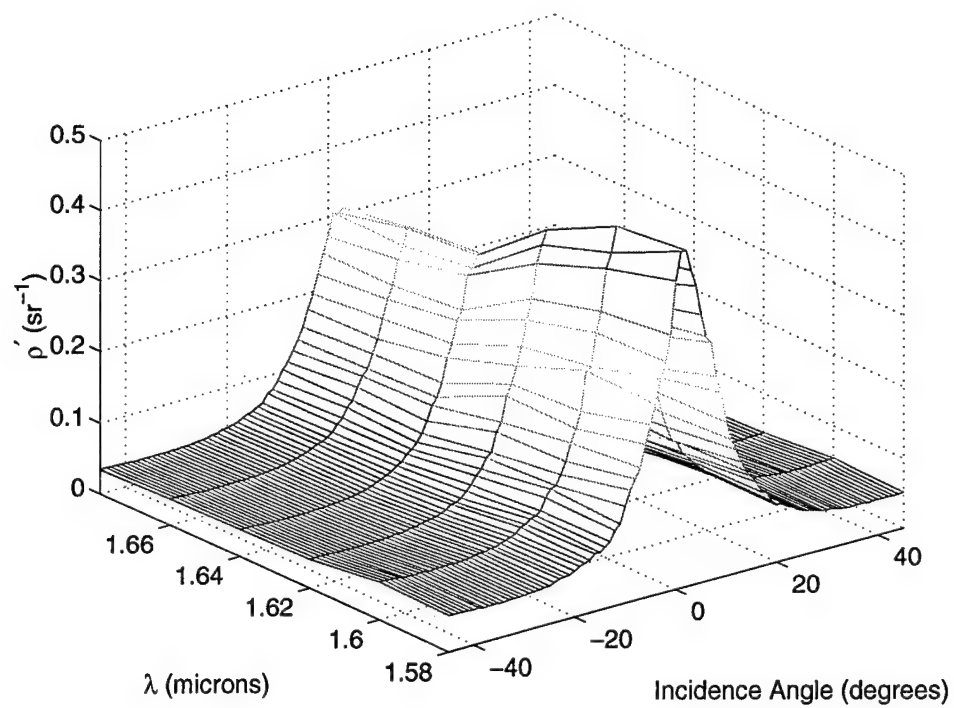


(a)

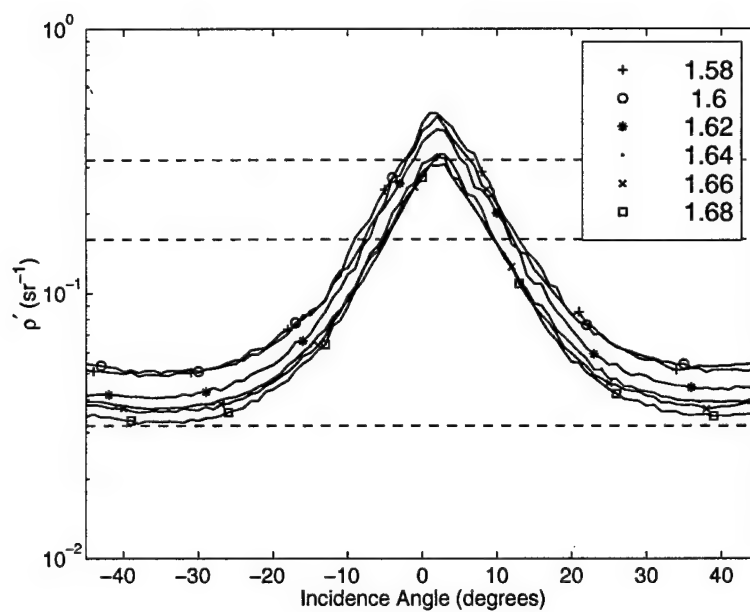


(b)

Figure 34 RC Method: D-08 BRDF data.



(a)



(b)

Figure 35 RC Method: E-38 BRDF data.

Appendix C. Matlab Code for Correlation Band Selection Algorithm

C.1 CBand Selection Script

```
% Script: cbandsel
% This script performs band selection using a correlation technique
clear all
close all

% Set up Matlab for B&W plots
set(0,'DefaultAxesColorOrder',[0 0 0],...
    'DefaultAxesLineStyleOrder','-|-.|--|:',...
    'DefaultAxesFontSize',14,...
    'DefaultLineLineWidth',1);

%-----%
% Loads NEFTXT reflectance spectra from a set of classes of %
% materials. Load the atmosphere data which is sampled %
% at the same wavelengths. Then compute the best bands %
% for class discrimination. %
%-----%
data=readcfg('4class.cfg');
fname=data(:,1); % filenames from config file
SUBNAMES=data(:,2); % Names for each subclass
ftype=data(:,3); % Type of file... NEF, JHU, etc

[NC,temp]=size(SUBNAMES); % # of classes

%-----%
% Load MODTRAN atmospheric transmission %
% which has already been converted into %
% MATLAB format. 0.82-5 um with 210 samp %
%-----%
load DATA/atmos.mat
% square to get round trip transmission!
atmA=atmA.^2;
%atmA=ones(size(atmA)); % uncomment to remove atmospheric effects

figure(1);
plot(linspace(.82,5,210),atmA)
xlabel('\lambda (microns)');
ylabel('Transmission');
axis([1,5,0,1]);

%-----%
% Load the class spectral data from the config %
% file names(reflectances and wavelengths) %
```

```

%------%
for i=1:NC
    fn=char(fname(i));
    switch char(ftype(i))
        case 'NEF'
            eval(sprintf('S(%d,:),w]=loadnefraw(\'\'%s\')\');',i,fn));
        case 'JHU'
            eval(sprintf(' [temp,w]=loadjhutxt(\'\'%s\')\');',fn));
            eval(sprintf('S(%d,:)=temp\';',i));
        case 'NEFbare'
            eval(sprintf(' [S(%d,:),w]=loadnefrawbare(\'\'%s\')\');',i,fn));
    end
    % Take atmospheric transmission into effect
    eval(sprintf('SS(%d,:)=S(%d,:);',i,i));
    eval(sprintf('S(%d,:)=S(%d,:).*atmA\';',i,i));
end

%------%
% Plot spectra -- both with and without atmospheric effects %
%------%
figure(2);
set(gca,'ColorOrder',[0 0 0]);
bp=plot(w',SS');
axis([1,max(w),0,1.1*max(max(SS))]);
title('Class Reflectance Spectra');
xlabel('\lambda (microns)');
ylabel('Reflectance');
legend(bp,char(SUBNAMES))

figure(3);
b=plot(w',S');
axis([1,max(w),0,1.1*max(max(S))]);
title('Class Reflectance Spectra w/ Curr. Modeled Atmos Transmittance ');
xlabel('\lambda (microns)');
ylabel('Reflectance');
legend(b,char(SUBNAMES))

%------%
% Do Band Selection %
%------%
% specify start and end bands for consideration
% 10=1.0 microns, 35=1.5 microns, 110=3.0 microns, 210=5.0 microns
% 85=2.5 microns

st=10; % start band
st=1;
ed=210; % end band

% Put all spectral data into one matrix S
S=S(:,st:ed);

```

```

wlen=w(st:ed); % make a wavelength vector that is the same size as S

% Now only include wavelengths with atmospheric transmission of
% at least atmstx but still use the reflectance data with no atmospheric
% correction for picking bands. i.e. Use atmospheric transmission to
% disclude bands with low transmission but don't let the shape of the
% atmospheric transmission curves determine the lowest correlation point

atmstx=.1;
indx=find(atmA>atmstx);
S=S(:,indx);
SS=SS(:,indx);
wlen=wlen(indx);

% build up the correlation matrix
cm=corrmat(SS,'ss');

% find the two bands which are least correlated
[temp1,temp2]=find(cm==min(min(cm)));
b1=temp1(1);
b2=temp1(2);

maxband=[b1,b2];

% now find the third band which is farthest from (t1,t2) in this space
% given b1 and b2
numbands=5;
for j=3:numbands
    % build up matrix to check for max dist
    Ta=[]; % holds correlations of chosen bands with all other bands
    T=[]; % holds autocorrelations of chosen bands
    for i=1:length(maxband)
        Ta=[Ta; cm(maxband(i),:)];
        T=[T; cm(maxband(i),maxband(i))*ones(size(cm(maxband(i),:)))];
    end

    % loop through to find max dist from (t1,t2)
    nbands=length(Ta);

    % find the distance from each set of points to the autocorrelations
    D1=sqrt(sum((Ta-T).^2));
    %D1=sqrt(sum(Ta.^2));

    % sort D1 least to greatest for ranking selection
    [D1sort,place]=sort(D1);
    % start at end (largest D1) and find index of first band not already used
    found=0; k=0;
    while ~found
        if isempty(find(place(end-k)==maxband))
            found=1;
            indx2=place(end-k);
        end
    end
end

```

```

        end
        k=k+1;
    end
    %plot(D1);
    %hold on;
    maxband=[maxband indx2];
    %pause;
end
hold off;
wlen(maxband)

figure(4);
plot(Ta(1,:),Ta(2,:),'.');
hold on;
plot(T(1),T(2),'s','MarkerFaceColor',[.5 .5 .5],'MarkerSize',7);
plot(Ta(1,maxband(3)),Ta(2,maxband(3)),'^','MarkerFaceColor',...
[.5 .5 .5],'MarkerSize',7);
hold off;
axis square;
xlabel('Cross-correlation w/ B1');
ylabel('Cross-correlation w/ B2');

% Add lines to plots to show selected bands
figure(2); line([wlen(maxband);wlen(maxband)],...
[zeros(1,length(maxband));ones(1,length(maxband))],...
'LineStyle','-','Color',[.25 .25 .25]);

figure(3); line([wlen(maxband);wlen(maxband)],...
[zeros(1,length(maxband));ones(1,length(maxband))],...
'LineStyle','-','Color',[.25 .25 .25]);

figure(5); plot(wlen,SS,'.'); axis ([1,5,0,1]);
xlabel('\lambda (microns)');
ylabel('Reflectance');
axis([1,5,0,.6]);
line([wlen(maxband);wlen(maxband)],...
[zeros(1,length(maxband));ones(1,length(maxband))],...
'LineStyle','-','Color',[.25 .25 .25]);

```

C.2 Supporting Functions

Function: Readcfg.m.

```
function names=readcfg(filename)
% this reads in the config file and loads up spectral data

if nargin<1
    filename='orig.cfg';
end

fid=fopen(filename);

samps=str2num(fgetl(fid));
names={};

for i=1:samps
    str=fgetl(fid);

    % Now parse it
    [token,str]=strtok(str);
    names(i,1)={token};
    [token,str]=strtok(str,'\''');
    [token,str]=strtok(str,'\''');
    names(i,2)={token};
    [token,str]=strtok(str);
    [token,str]=strtok(str);
    names(i,3)={token};
end

fclose(fid);
```

Function: Corrmat.m.

```
function cmat=corrmat(S,method)
% Useage: cmat=corrmat(S,method)
% Purpose: This function builds the correlation matrix for the matrix S
% Inputs:
% S = Row ordered set of reflectance values
% method = normalization method used in normcorr (ss or ms)
% Outputs:
% cmat = normalize correlation matrix for all combinations of the bands
% Written by: Capt Brad Rennich
% 19 Dec 98

[nclass,nbands]=size(S);

% build a cmat of the right size
cmat=ones(nbands,nbands).*NaN;

% fill up correlation matrix
for i=1:nbands
    for j=1:nbands
        cmat(i,j)=normcorr(S(:,[i,j]),method);
    end
end
end
```

Function: Normcorr.m.

```
function nc=normcorr(S,method)
% Usage: nc=normcorr(S,method)
% Purpose: This function calculates the "normalized correlation"
% of the matrix S
% Inputs:
% S : a row ordered set of vectors in which each set is a row
%     and each col is a different wavelength
% method: method to use for normalization step
% ss = straight scale -- scale about zero
% ms = mean scale -- scale about the mean
% Outputs:
% nc: a single number ranging between 0 and 1
% 1 =
% Written By: Capt Brad Rennich
% Date:      18 Dec 98

[nclass,nbands]=size(S);

if strcmp(method,'ss')
    % ***** Straight scaling for normalization *****%
    % first normalize each band so highest reflectance value is 1
    Smax=max(S);

    for i=1:nbands
        S(:,i)=S(:,i)./Smax(i);
    end

    % *****%
end

if strcmp(method,'ms')
    % ***** Normalize about the mean *****%
    Sm=mean(S);

    % Subtract the mean of each band and stretch so range is 1
    for i=1:nbands
        S(:,i)=S(:,i)-Sm(i);
        S(:,i)=S(:,i)./(max(S(:,i))-min(S(:,i))));
    end

    Smin=min(S);

    for i=1:nbands
        S(:,i)=S(:,i)-Smin(i);
    end
```

```
% *****%  
end  
  
% now find normalized correlation  
nc=(sum(S(:,1).*S(:,2)))./nclass;
```

Bibliography

1. Bevington, Philip R. and D. Keith Robinson. *Data Reduction and Error Analysis for the Physical Sciences* (Second Edition). McGraw-Hill, Inc., 1992.
2. Csillag, Ferenc, et al. "Spectral Band Selection for the Characterization of Salinity Status of Soils," *Remote Sensing of the Environment*, 43:231-242 (1993).
3. Driscoll, Walter G. and William Vaughan, editors. *Handbook of Optics*. McGraw-Hill, Inc., 1978.
4. Fukunaga, Keinosuke. *Introduction to Statistical Pattern Recognition* (Second Edition). Academic Press, Inc., 1990.
5. Hardie, Russell C., et al. "Spectral Band Selection and Classifier Design for a Multispectral Imaging Laser Radar," *Optical Engineering*, 37:752-762 (Feb 1998).
6. Hecht, Eugene. *Optics* (Second Edition). Addison-Wesley Publishing Company, Inc., 1987.
7. Jelalian, Albert V. *Laser Radar Systems*. Artech House, 1992.
8. Musikant, Solomon. *Optical Materials*. Marcel Dekker, Inc., 1985.
9. Office of Research and Development (ORD). *Nonconventional Exploitation Factors Data System (NEFDS) Specifications* (Ord 258-96 Edition), August 1996.
10. Price, John C. "Band Selection Procedures for Multispectral Scanners," *Applied Optics*, 33(15):3281-3288 (May 1994).
11. Satyshur, M. P., et al. "Multispectral Imaging: Band Selection and Performance Predictions," *IRIS Speciality Group on Targets, Backgrounds, and Discrimination*, 1:425-434 (Feb 1997).
12. Schowengerdt, Robert A. *Remote Sensing, Models and Methods for Image Processing* (Second Edition). Academic Press, 1997.
13. Schwartz, Craig R., et al. "Thermal Multispectral Detection of Military Vehicles in Vegetated and Desert Backgrounds," *SPIE*, 2742:286-297 (1996).
14. Stover, John C. *Optical Scattering: Measurement and Analysis*. McGraw-Hill, Inc., 1990.
15. Thomas, David J., et al. "Bidirectional Reflectance Measurements for High-Resolution Signature Modeling," *SPIE*, 3062:105-116 (1997).
16. Vaidyanathan, Mohan, et al. "Tunable 1.3 to 1.5 μm wavelength target reflectance measurement system." Draft copy.
17. Wilbur B. Davenport, Jr. *Probability and Random Processes An Introduction for Applied Scientists and Engineers*. McGraw-Hill, Inc., 1987.
18. Yariv, Amnon and Pochi Yeh. *Optical Waves in Crystals* (Second Edition). John Wiley & Sons, Inc., 1984.

Vita

Captain Bradley D. Rennich was born on 6 October 1970 in White, SD. He graduated from Deubrook High School in White, South Dakota in 1989. He attended South Dakota State University and was awarded the Bachelor of Science degree in Electrical Engineering in May 1994. He received his commission through the Detachment 780 AFROTC at South Dakota State University.

His first assignment was at Kirtland AFB, NM in the Phillips Laboratory Airborne Experiments Branch as an electronics integration engineer. In January 1996, he transitioned to the Argus Flight Test Branch where he worked as a flight test engineer in charge of the Argus payload computer systems. In August 1997 he was assigned to Wright-Patterson AFB to pursue a Master of Science degree in Electrical Engineering at the Air Force Institute of Technology with a speciality in electro optics. He is a member of IEEE and Eta Kappa Nu. Brad is married to Julie (Roelofsen) Rennich. They have two children.

Permanent address: 20347 475th Ave.
White, SD 57276

REPORT DOCUMENTATION PAGE			Form Approved OMB No. 0704-0188	
Public reporting burden for this collection of information is estimated to average 1 hour per response, including the time for reviewing instructions, searching existing data sources, gathering and maintaining the data needed, and completing and reviewing the collection of information. Send comments regarding this burden estimate or any other aspect of this collection of information, including suggestions for reducing this burden, to Washington Headquarters Services, Directorate for Information Operations and Reports, 1215 Jefferson Davis Highway, Suite 1204, Arlington, VA 22202-4302, and to the Office of Management and Budget, Paperwork Reduction Project (0704-0188), Washington, DC 20503.				
1. AGENCY USE ONLY (Leave blank)		2. REPORT DATE 1 March 1999		3. REPORT TYPE AND DATES COVERED Masters Thesis
4. TITLE AND SUBTITLE Active Multispectral Band Selection and Reflectance Measurement System			5. FUNDING NUMBERS	
6. AUTHOR(S) Bradley D. Rennich, Captain, USAF				
7. PERFORMING ORGANIZATION NAME(S) AND ADDRESS(ES) Air Force Institute of Technology School of Engineering 2950 P St. WPAFB, OH 45433-7765			8. PERFORMING ORGANIZATION REPORT NUMBER AFIT/GEO/ENP/99M-01	
9. SPONSORING/MONITORING AGENCY NAME(S) AND ADDRESS(ES) AFRL/SNJ (Maj Pat Gardner) 2241 Avionics Cir WPAFB, OH 45433-7304			10. SPONSORING/MONITORING AGENCY REPORT NUMBER	
11. SUPPLEMENTARY NOTES				
12a. DISTRIBUTION AVAILABILITY STATEMENT Approved for Public Release; Distribution Unlimited			12b. DISTRIBUTION CODE	
13. ABSTRACT (Maximum 200 words) <p>Due to system design requirements, an active multispectral laser radar system may be limited in the number of spectral bands that can be integrated into the system. To aid in the selection of these bands, a novel multispectral band selection technique is presented based on the cross-correlation of the material class reflectance spectra over a wavelength range of 1 - 5 microns. The algorithm uses directional hemispherical reflectance data from the Nonconventional Exploitation Factors database to select a number of spectral bands for classification purposes.</p> <p>Because the target material spectral reflectance is so important to the performance of an active multispectral system, an experimental monostatic bidirectional reflectance distribution function (BRDF) measurement system is developed and tested. A 1.06 micron Nd:YAG diode pumped laser is frequency shifted to 1.58 - 1.80 microns using a periodically poled lithium niobate nonlinear crystal. This laser provides the continuously tunable source necessary to measure the material BRDF at closely spaced wavelength intervals. A complete error analysis of the system is presented with measurement results from a number of military vehicle paint samples. An extended design is presented which is capable of operating at any wavelength in the 1 - 5 micron range. This design also reduces or removes the error sources observed in the initial experiment.</p>				
14. SUBJECT TERMS bidirectional reflectance distribution function (BRDF), spectral band selection, multispectral			15. NUMBER OF PAGES 88	
			16. PRICE CODE	
17. SECURITY CLASSIFICATION OF REPORT Unclassified	18. SECURITY CLASSIFICATION OF THIS PAGE Unclassified	19. SECURITY CLASSIFICATION OF ABSTRACT Unclassified	20. LIMITATION OF ABSTRACT UL	